Information Processing and Management 58 (2021) 102411

Contents lists available at ScienceDirect

Information Processing and Management

journal homepage: www.elsevier.com/locate/infoproman

CGNet: A graph-knowledge embedded convolutional neural network for detection of pneumonia

Xiang Yu[a], Shui-Hua Wang[b,*], Yu-Dong Zhang[a,c,*]

[a] School of Informatics, University of Leicester, Leicester, LE1 7RH, UK
[b] School of Architecture Building and Civil engineering, Loughborough University, Loughborough, LE11 3TU, UK
[c] Department of Information Systems, Faculty of Computing and Information Technology, King Abdulaziz University, Jeddah 21589, Saudi Arabia

ARTICLE INFO

Keywords:
COVID-19
Chest X-ray images
Transfer learning
Graph
Feature reconstruction

ABSTRACT

Pneumonia is a global disease that causes high children mortality. The situation has even been worsening by the outbreak of the new coronavirus named COVID-19, which has killed more than 983,907 so far. People infected by the virus would show symptoms like fever and coughing as well as pneumonia as the infection progresses. Timely detection is a public consensus achieved that would benefit possible treatments and therefore contain the spread of COVID-19. X-ray, an expedient imaging technique, has been widely used for the detection of pneumonia caused by COVID-19 and some other virus. To facilitate the process of diagnosis of pneumonia, we developed a deep learning framework for a binary classification task that classifies chest X-ray images into normal and pneumonia based on our proposed CGNet. In our CGNet, there are three components including feature extraction, graph-based feature reconstruction and classification. We first use the transfer learning technique to train the state-of-the-art convolutional neural networks (CNNs) for binary classification while the trained CNNs are used to produce features for the following two components. Then, by deploying graph-based feature reconstruction, we, therefore, combine features through the graph to reconstruct features. Finally, a shallow neural network named GNet, a one layer graph neural network, which takes the combined features as the input, classifies chest X-ray images into normal and pneumonia. Our model achieved the best accuracy at 0.9872, sensitivity at 1 and specificity at 0.9795 on a public pneumonia dataset that includes 5,856 chest X-ray images. To evaluate the performance of our proposed method on detection of pneumonia caused by COVID-19, we also tested the proposed method on a public COVID-19 CT dataset, where we achieved the highest performance at the accuracy of 0.99, specificity at 1 and sensitivity at 0.98, respectively.

1. Introduction

Pneumonia is a common yet serious lung disease caused by viruses and bacteria. Though it is treatable under most situations, timely detection still plays a key role in making diagnosis and treatment. Since the outbreak of COVID-19, Viral nucleic acid techniques (VNATs) and imaging techniques have been widely used to quickly diagnose pneumonia caused by COVID-19. It was reported that the sensitivity of VNATs was high (Behzadi, Ranjbar & Alavian, 2014), the false positive rate, however, is relatively high when compared to imaging-based detection methods (Fang et al. 2020). As pointed out by authors in Fang et al. (2020), a VNAT using real-time

* Corresponding authors.
E-mail addresses: xy144@le.ac.uk (X. Yu), shuihuawang@ieee.org (S.-H. Wang), yudongzhang@ieee.org (Y.-D. Zhang).

https://doi.org/10.1016/j.ipm.2020.102411
Received 20 June 2020; Received in revised form 26 September 2020; Accepted 10 October 2020
Available online 19 October 2020

polymerase chain reaction (RT-PCR) achieved a sensitivity at 71% on a 51 cases dataset, however, Chest computed tomography (CT) showed sensitivity at 98%. Chest X-ray imaging has also been extensively deployed for the detection of pneumonia caused by COVID-19 (Adhikari, 2020; Islam, Wijewickrema, Collins & O'Leary, 2020; Rajpurkar et al., 2017). Compared to VNATs, Chest X-ray imaging is more accurate and convenient, which makes Chest X-ray to be the most popular technique for diagnosis of pneumonia (Chen et al., 2019). Also, compared to CT, X-ray is more popular because of the low cost and convenience of imaging. However, manual interpretation of the digitalized images, a time-consuming task, remains to be a challenging job for the radiologists due to the complexity and artificial factors. Therefore, automatic systems that can help radiologists with the understanding of images is demanding and would be greatly helpful to slow the spreading of COVID-19.

Deep learning (DL), a fast-developing branch of Machine Learning (ML), has shown great power over image classification and detection. Compared to classical ML methods, which heavily rely on manually crafted features, Deep Convolutional Neural Networks (CNNs), the most typical models of DL, have achieved eye-attracting success on considerable image-based tasks such as detection, classification and segmentation (He, Zhang, Ren & Sun, 2016; Ronneberger, Fischer & Brox, 2015; Zhao, Zheng, Xu & Wu, 2019). DL models, which are usually trained on millions of images, learn more abstract features than traditional ML models that focus on learning more straightforward but less representative features. Therefore, DL models have been showing huge advantages over traditional ML models on accuracy, flexibility and robustness. In some areas, DL models even outperformed the experts in the area by a large margin He Kaiming, Shaoqing and Jian (2016); He, Zhang, Ren and Sun (2015). Given the stated superiority, DL techniques have been embedded in many Computer-aided (CAD) systems. For DL systems, how to effectively embed useful information into the systems determines the final performance of the systems. There are considerable research works on information embedding (Li, Zhang, Qin, Zhang & Shao, 2019; Shen et al., 2021; Wen, Zhang, Zhang, Fei & Wang, 2020; Zhang et al., 2019, 2020; Zhang, Liu, Shen, Shen & Shao, 2018).

In this research, we proposed a new DL model named CGNet framework, which was featured by the proposed feature reconstruction method. Based on the proposed framework, a new high-performance pneumonia detection system was developed. In our proposed CGNet framework, there are three modules including feature extraction and graph-based feature reconstruction and classification. For the feature extraction, we transferred the state-of-the-art networks and trained with pneumonia datasets. High-level features, which are coarse features for further classification, can then be acquired through the trained networks. Based on the extracted features, we propose to integrate graph representation between individual images to improve the accuracy of the following classifier GNet, which has the same architecture as the artificial neural network(ANN) but outperforms ANN by a large margin. Contrary to traditional ANN that analyses images individually, our proposed GNet can utilize the underlying relationship between images to contribute to better classification performance and therefore analyse multiple images simultaneously. The architecture of GNet is designed to be shallow to avoid the overfitting problem and unnecessary over-complexity of the whole system. Features of each image are taken as a node in graphs while edges between nodes are assigned to top k neighbours that have the shortest distance to the node. To validate our models designed according to the newly proposed framework, we evaluated the performance of models on a public X-ray pneumonia dataset as well as a public CT-image COVID-19 dataset. As being shown in the experiment, our developed system showed promising results on a public pneumonia dataset with more than 5000 images while the developed system reached an accuracy at 0.99 on the public COVID-19 dataset. Like pneumonia caused by other bacteria and viruses will cause inflammation and the air sacs, or alveoli in the lungs, COVID-19 caused pneumonia shows similar symptoms (Koo et al., 2018; Li et al., 2020). Therefore, we believe that the developed system could be helpful for the diagnosis of pneumonia caused by COVID-19 and other causes in future.

The paper is arranged as follows: In Section 2, we will briefly review the related work concerning CAD systems for the detection of pneumonia. Our proposed framework will be presented in detail in Section 3, followed by experiments in Section 4. Discussion is given in Section 5 as we conclude this paper in Section 6.

2. Related work

Feature reconstruction has been proved to be effective in improving the performance of feed-forward deep neural network (Chung, Park & Jung, 2019). When considering a feature reconstruction problem, the target feature matrix $T_t \in \mathbb{R}^{n\times m}$can be denoted by informative components $I_t \in \mathbb{R}^{n\times m}$and trivial components $Tr_t \in \mathbb{R}^{n\times m}$.

$$T_t = I_t + Tr_t \tag{1}$$

Principle Component Analysis (PCA) is a widely deployed technique for feature dimension reduction and reconstruction (Malagón-Borja & Fuentes, 2009). Given a group of features F_i ($i \in \mathbb{R}^N$, $N$is the number of features in the group), the mean feature $\overline{F}_i$can then be expressed as:

$$\overline{F}_i = \sum_{j=1}^{N} F_i \tag{2}$$

The covariance matrix C is then given by

$$C = \sum_{j=1}^{N} \left(F_i - \overline{F}_{ii}\right)\left(F_i - \overline{F}_i\right)^T \tag{3}$$

After calculating the eigenvalues and eigenvectors, the features F_i can be reconstructed by selecting the first k eigenvectors which

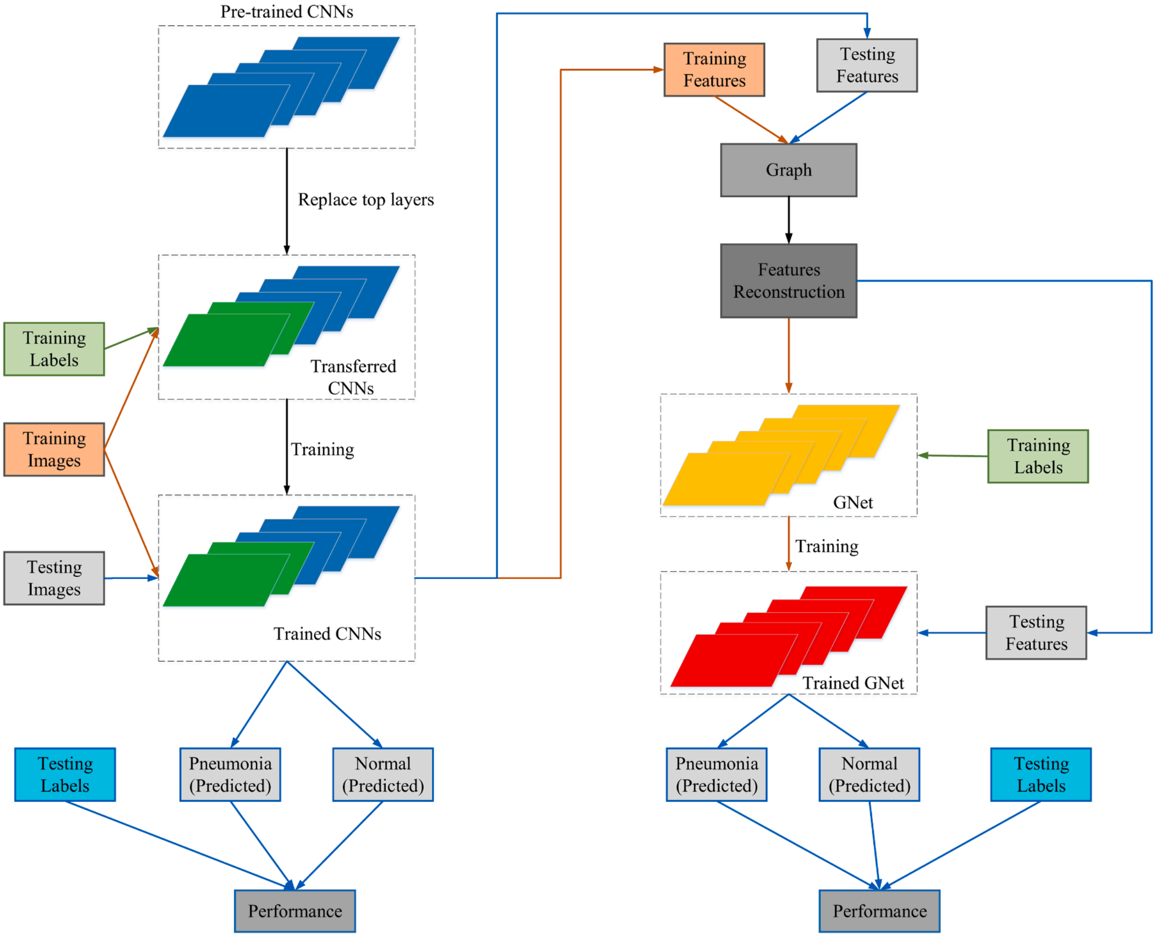

Fig. 1. The flow chart of the proposed framework.

correspond to the first biggest k eigenvalues. DL has been experiencing fast development and wide utilization in different areas, especially in the past few years. Also, many CAD systems for image analysis have used DL technique due to the excellent performance of DL. Therefore, it is heuristic to combine feature reconstruction with DL technique for the exploration of the better-performed image analysis system. Since the outbreak of COVID-19, experts in computer science community have been working hard to develop CAD systems for the detection of pneumonia caused by COVID-19, which helps to detect COVID-19.

In many of those works, transfer learning is prevalently used due to its advantages. Usually, training a deep CNN from scratch takes a long time while the performance of the trained CNN could be far from satisfaction. Therefore, transfer learning, a technique that reuses existing resolutions for new tasks, can then be used to build CNN models more effectively. In transfer learning, base networks are networks trained on different datasets, usually on ImageNet. The architectures of base networks are adjusted correspondingly to meet the specific image analysis tasks. The adjusted networks can then be trained by the interested datasets. Also, the base networks can be used as feature extractors that provide extracted features for classifiers. Given the stated advantages of transfer learning, transfer learning has been used in the detection of pneumonia. For example, a deep transfer learning model named ChestNet was proposed for the detection of multiple thorax diseases including pneumonia (Wang & Xia, 2018). The authors used ResNet architecture as the backbone, which achieved an average area under the curve (AUC) at 0.7810 per-class on X-ray images. The model was implemented under CAFFE framework (Jia et al., 2014) while it was trained on a high-performance configuration. Another similar transfer-learning-based work can be found at (Rajpurkar et al., 2017). Based on DenseNet, a model named CheXNet was proposed for detection of pneumonia based on X-ray images. The performance of the proposed model even surpassed the average performance of radiologists. Since the outbreak of COVID-19, there are also considerable works on the detection of pneumonia caused by it. To validate the performance of AI on the detection of COVID-19, authors in Chowdhury et al. (2020) explored the performance of the state-of-the-art CNNs on the detection task. In their work, they transferred AlexNet, SqueezeNet, ResNet-18 and DenseNet201 (He et al., 2016; Huang, Liu, Van Der Maaten & Weinberger, 2017; Iandola et al., 2016; Krizhevsky Alex, 2012), amongst which SqueezeNet showed the best performance on an augmented dataset. Before augmentation, there are 190 COVID-19, 1345 viral pneumonia, and 1341 normal X-ray images in the original dataset. 130 X-ray images from 190 COVID-19 were randomly selected into the training set. To balance the samples in the dataset, each category of images was then augmented to around 2600. Rotation, scaling and

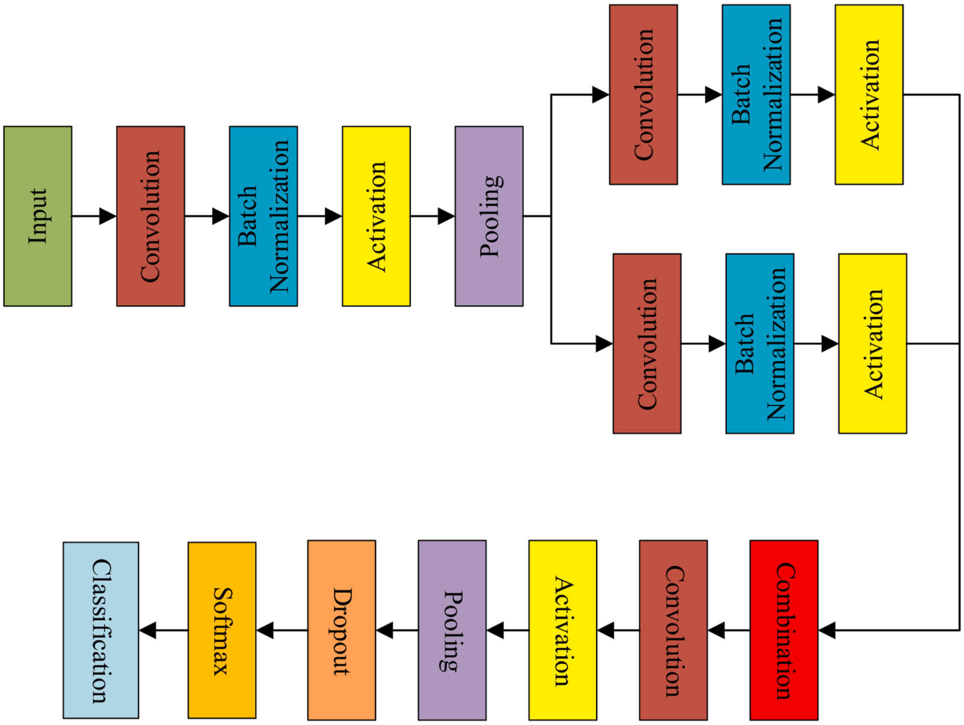

Fig. 2. General architecture of CNNs.

translation were three augmentation methods applied. The reported highest accuracy, sensitivity and specificity in the work were 98.3%, 96.7%, and 100%. However, only 60 COVID-19 positive X-ray images were analysed in the test set. In another work (Joaquin, 2020), a so-called Inception CNN was transferred on a dataset that comprises of 1119 Computerized Tomography (CT) scans (Szegedy Christian et al., 2015). The proposed model showed promising results on the internal and external dataset with the accuracy of 89.5% and 79.3% respectively, which remains to be improved to meet practical requirements. Inception has also been introduced in the work (Wang et al., 2020). 453 confirmed COVID-19 images were analysed while 217 images were partitioned into the training set. The author claimed that deep learning is of great significance on extracting graphical features for diagnosis of COVID-19 as the proposed model showed an overall accuracy at 73.1% on the external dataset. Some other valuable works in the area can be found at (Abbas, Abdelsamea & Gaber, 2020; Apostolopoulos & Mpesiana, 2020; Bukhari, Bukhari, Syed & SHAH, 2020).

One common problem in the detection of pneumonia by CAD systems is the lack of large-scale public datasets. While many works reported high performance, the numbers of images in the testing datasets are too few to form convincing results. Also, many of the works simply transferred the state-of-the-art CNNs to the classification task without further exploration of structural optimization while the reported performance heavily relies on the pre-determined parameters and hardware. To solve the stated issues, we proposed our CGNet framework to detect pneumonia based on large scale public X-ray datasets. Evaluation of a public COVID-19-caused pneumonia CT dataset also supported the proposed method. In the proposed framework, we first transferred the state-of-the-art CNNs for feature extraction instead of direct classification. Graph representations of extracted features are constructed based on the similarities of the features, which was measured by Euclidean distance between features. Each feature is then taken as a node in a graph while edges between nodes are connected when nodes were found to be neighbours according to Euclidean distance. The combined features are used for classification by our GNet, a simple graph neural network. Experiments on a public chest X-ray image dataset showed that our system implemented under CGNet framework surpassed the majority of the state-of-the-art methods while the sensitivity was extremely high.

3. Methodology

In general classification tasks, features of data are first extracted and then be classified by classifiers in traditional ML methods. In our proposed CGNet framework, there are mainly three individual components that correspond to feature extraction, feature reconstruction and final classification respectively. However, unlike traditional ML methods, which heavily rely on manually-crafted features, our framework extracts high-level abstract features by transferring the state-of-the-art CNNs in the first step. Graph representations are then delved into depth according to features‘ Euclidean distance. Finally, the classifiers are trained with features embedded with graph representation. The data flow of the proposed model under CGnet framework can be seen in Fig. 1.

In Fig. 1, the procedures on obtaining trained CNNs is shown in left. The dark greened layers shown in transferred CNNs and trained CNNs are new top layers that replace original top layers in CNNs. The arrows in orange and blue show the flows of the training set and

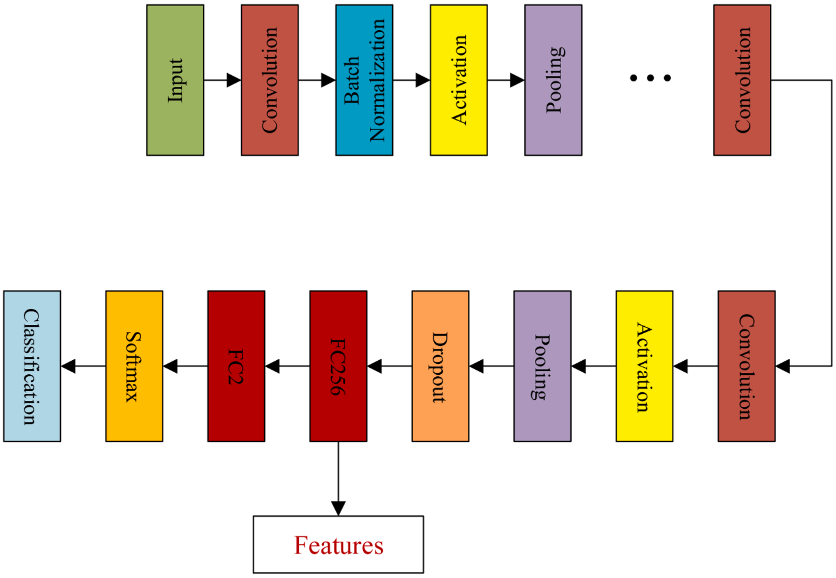

Fig. 3. Architecture of transferred CNNs. FC256 and FC2 stand for fully connected layers with 256 and 2 channels respectively.

Algorithm 1
Feature acquisition.

```
Stage 1: Network transferring
Step 1.1: Load pre-trained state-of-the-art networks; (trained on ImageNet;)
Step 1.2: Remove the Softmax layer and classification layer;
Step 1.3: Add new layers including dropout, FC256, FC2, new Softmax layers, and new classification layers;
Step 1.4: Train new networks on the training set of pneumonia dataset with predefined parameters;
Step 1.5: Save trained networks and parameters;
Stage 2: Feature extraction
Step 2.1: Load trained networks;
Step 2.2: Input the dataset to trained networks for feature extraction;
Step 2.3: Extract features produced by fully-connected layer FC256.
```

the test set. When implementing our models for pneumonia detection under CGNet framework, we choose CNNs that performed best on the test set as feature extractors. GNet, which takes features combined with graph representations as input, finally classifies images into normal and pneumonia. We will have a detailed illustration of each component as follows.

3.1. Feature extraction by transferred CNNs

Unlike traditional ML methods that utilize manually-designed algorithms for ad hoc tasks, we use deep- learning-based algorithms that have a higher superiority on generalization. Feature extraction plays a key role in the classification task, which directly determines the overall performance of the following classifiers. Primarily, we implement feature extraction by deploying transfer learning technique. In our feature extraction stage, the state-of-the-art networks are first transferred to the binary classification task by replacing top layers with new layers. After training with the training set, CNNs that can provide preliminary results as well as features. Generally, CNNs are trained on ImageNet (Deng et al., 2009) that give 1000-categories classification results. The general architecture of CNNs is given in Fig. 2. After transferred the state-of-the-art networks, we chose the CNN that gives the best result on the test set as a feature extractor for following GNet.

To transfer CNNs pre-trained on ImageNet, we first removed the top layers of CNNs and then added new layers including one dropout layer, one transitional fully-connected layer with 256 channels and the final 2 channel fully-connected layer for classification. Dropout layer is added to prevent overfitting problem during the training session. Information of features would suffer from significant loss if the dimensions of feature shrink rapidly. Therefore, a transitional fully-connected layer is placed on the top of the dropout layer to prohibit heavy information loss. The detailed architecture of transferred CNNs can be seen in Fig. 3, where FC256 and FC2 stand for two fully-connected layers with 256 and 2 channels respectively. The connection between the final pooling layer and Softmax layer is replaced by the connection between the final pooling layer and newly added dropout layer. After training the transferred networks with pneumonia dataset with a limited number of epochs, the parameters within CNNs are fine-tuned towards the desired parameters that give better representations of the dataset. The details about the acquisition of features under our framework can be found in Algorithm 1, which includes two states that are network transferring and feature extraction, where the extracted features are analysed

Algorithm 2
Graph generation.

```
Divide features into batches;
For each batch of features, let each feature in the batch be the node;
Calculate the Euclidean distance between each node to the rest nodes in the graph;
Find nearest $k$ neighbours for each node;
Assign a positive value at positions that correspond to $k$ neighbours.
```

Algorithm 3
Acquisition of adjacency matrix A_i.

```
Step 1: Initialization (See Eqs. (7)-10)
Initialize adjacency matrix $\boldsymbol{A_i}$;
Initialize distance between features $\boldsymbol{Distance}$;
Initialize variable $\boldsymbol{Sorted\_Distance}$ for sorted distance;
Initialize variable $\boldsymbol{Index}$;
Step 2: Distance calculation
for $\boldsymbol{a} = 1{:}S$
for $\boldsymbol{b} = 1{:}S$
if $\boldsymbol{a}\,!\!=\boldsymbol{b}$
$\boldsymbol{Distance}(\boldsymbol{a},\boldsymbol{b}) = \mathrm{sum}(f_a - f_b)$;
end
end
end
Step 3: Output $\boldsymbol{A_i}$
for $\boldsymbol{a} = 1{:}S$
$[\boldsymbol{Sorted\_Distance}(\boldsymbol{a},:),\ \boldsymbol{Index}(\boldsymbol{a},:)] = \mathrm{sort}(\boldsymbol{Distance}(\boldsymbol{a},:))$;
for $c = 1{:}k$
$\boldsymbol{A}_i(\boldsymbol{a},\boldsymbol{Index}(\boldsymbol{a},\boldsymbol{c})) = 1$;
end
end
then output $\boldsymbol{A_i}$.
```

for underlying graph representation.

3.2. Graph embedded feature reconstruction

We use graph information extracted from features to reconstruct the features. The reason why we do this is that individual feature will be enhanced when reconstructed by neighbour features. Features here refer to features extracted by trained CNNs. To build graphs of features, each feature extracted from each image is taken as a node of the graphs. For efficient computation, features are partitioned into batches. Given the features $\boldsymbol{F} \in \mathbb{R}^{D\times M}$, where $D$is the number of features in the dataset and M is the dimension of the features. Let the batch size to be N, then the number of batches n can be denoted as:

$$n = \lceil D / N \rceil \tag{4}$$

where $\lceil \cdot \rceil$ is the ceiling operation. Then $\boldsymbol{F}$ can be rewritten as:

$$\boldsymbol{F} = \left[\boldsymbol{F}_1{}^T, \cdots, \boldsymbol{F}_i{}^T, \cdots, \boldsymbol{F}_n{}^T\right]^T (1 \leq i \leq n) \tag{5}$$

$$\boldsymbol{F}_i = \left[\boldsymbol{f}_1, \cdots, \boldsymbol{f}_j, \cdots, \boldsymbol{f}_s\right]^T (1 \leq j \leq s) \tag{6}$$

where$\boldsymbol{f}_j \in \mathbb{R}^{M\times\ 1}$and $\boldsymbol{F}_i \in \mathbb{R}^{S\times M}$. Specifically, $\boldsymbol{f_j}$is the feature extracted by the previous component. For each $\boldsymbol{F_i}$, a corresponding graph $\boldsymbol{G_i} \in \mathbb{R}^M$that represents the underlying relationship between nodes by the paired variables ($\boldsymbol{V_i}$, $\boldsymbol{E_i}$) can be built. $\boldsymbol{V_i}$ stands for the nodes comprised of each feature $\boldsymbol{f_j}$ in the batch, while $\boldsymbol{E_i}$ is the edges between nodes. We believe edges exist between each node and its nearest k neighbours when k smallest Euclidean distance found. $\boldsymbol{E_i}$ is represented in a form of the adjacency matrix $\boldsymbol{A}_i \in \mathbb{R}^{S\times S}$. Given a node $\boldsymbol{f_j}$and its neighbour $\boldsymbol{f}_{j+1}$, the value at the position (j, $j + 1$) of $\boldsymbol{A_i}$ is set to be a positive number that shows two nodes are related. Hence, the key to build $\boldsymbol{G_i}$ is to calculate the adjacency matrix $\boldsymbol{A_i}$ (Liang & Bose, 1996). The procedures of graph generation can be seen in Algorithm 2.

When building graph $\boldsymbol{G_i}$ for each batch of features $\boldsymbol{F_i}$, we first calculate the distance between each feature to the rest features in the batch. By doing so, we can have a distance matrix $\boldsymbol{Distance} \in \mathbb{R}^{S\times S}$. After sorting each row of the acquired $\boldsymbol{Distance}$in ascending order, the corresponding index matrix $\boldsymbol{Index} \in \mathbb{R}^{S\times S}$that records the index of nearest k features in the batch $\boldsymbol{F_i}$ before sortation can be produced. For each row of $\boldsymbol{A_i}$, the value of one position in the row is set to 1 when the neighbour at the position is found to be one of the nearest k neighbours.

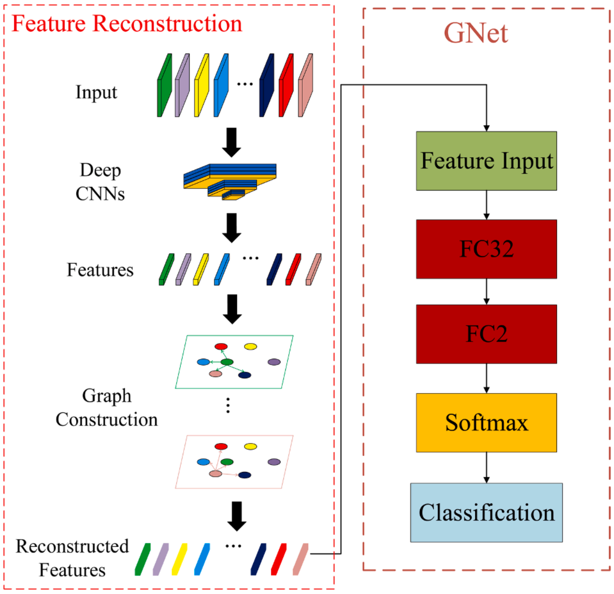

Fig. 4. Feature reconstruction and the architecture of GNet.

The pseudocode of acquisition of $\boldsymbol{A_i}$ can be found in Algorithm 3. At the initialization stages, the four variables are initialized as:

$$\boldsymbol{A}_i = \text{zeros}(S, S) \tag{7}$$

$$\boldsymbol{Distance} \;= \text{Infinity}(S, S) \tag{8}$$

$$\boldsymbol{Sorted\_Distance} = \text{zeros}(S, S) \tag{9}$$

$$\boldsymbol{Index} = \text{zeros}(S, S) \tag{10}$$

Specifically, the $\boldsymbol{Distance}$ is calculated according to:

$$\boldsymbol{Distance}(j, m) = \sqrt{\sum_{h=1}^{M} \left(f_j(h, 1) - f_m(h, 1)\right)^2} \tag{11}$$

After we calculated $\boldsymbol{A_i}$, each feature f_j in the batch $\boldsymbol{F_i}$ is reconstructed according to:

$$\boldsymbol{f}_j = \tilde{A}_i^j \boldsymbol{F}_i \tag{12}$$

$\tilde{A}_i^j$is the jth row of $\tilde{A}_i$, which is normalized adjacency matrix $\boldsymbol{A_i}$. Therefore, the reconstructed feature batch $\boldsymbol{F'}_{\boldsymbol{i}}$can be denoted as:

$$\boldsymbol{F}'_i = \tilde{\boldsymbol{A}}_i \boldsymbol{F}_i \tag{13}$$

When considering normalizing $\boldsymbol{A_i}$, we first calculate a degree matrix $\boldsymbol{D} \in \mathbb{R}^{S \times S}$, where:

$$\boldsymbol{D}(j, j) = \sum_{h=1}^{S} \boldsymbol{A}_i(j, h) \tag{14}$$

That is to say:

$$\boldsymbol{D}(j, h) = \begin{cases} k, & if\ j = h \\ 0, & if\ j! = h \end{cases} \tag{15}$$

We then normalize $\boldsymbol{A_i}$ by:

$$\tilde{\boldsymbol{A}}_i = \boldsymbol{D}^{-\frac{1}{2}}(\boldsymbol{A}_i + \boldsymbol{I})\boldsymbol{D}^{-\frac{1}{2}} \tag{16}$$

$\boldsymbol{I}$ is the identity matrix. After multiplying $\tilde{A}_i$with $\boldsymbol{F_i}$, we then have reconstructed feature batch $\boldsymbol{F'}_{\boldsymbol{i}}$ for classification. For pneumonia detection task, the reconstructed feature batches are input to the proposed GNet in the developed system.

Algorithm 4
Pseudocode of CGNet framework.

```
Loading CNNs pre-trained on ImageNet;
Remove top layers and add new top layers for the classification task;
Train the modified CNNs on the training dataset;
Obtain features through a fully-connected layer whose output size is 1000 from the trained CNNs;
Divide features into batches of same sizes;
Build graphs in each batch of features;
Reconstruct features according to graph information;
Train neural networks with reconstructed features;
Acquire features for test set by repeat Step 4 to Step 7 on the test set;
Test the trained neural networks with the reconstructed test features.
```

3.3. *GNet for classification*

We name our classifier as GNet when implementing our system for the detection of pneumonia because the proposed GNet is a single layer graph neural network where inputs are the nodes in the graph and the graph representations of the graph. In more general cases, traditional classifiers including ANN (Artificial Neural Network) and SVM (Support Vector Machine) can be used for classification based on extracted features.

Feature reconstruction procedures and architecture of GNet are shown in Fig. 4. In feature reconstruction, features mean the features extracted by the trained CNNs. In our scenario, GNet, which has the same structure as traditional ANNs, is different from traditional ANNs on input, where ANNs usually use features extracted with no postprocessing. The main reason why we don't introduce more hidden layers is that extra hidden layers will introduce an even large number of parameters, which could also trigger the overfitting problem. Also, we've obtained most representative features by reconstruction, and therefore only one hidden layer is introduced. The number of input channel is 256.

Given the expected output of batch $\boldsymbol{F_i}$ is $\boldsymbol{F_{Ei}}$ and the real output of GNet is $\boldsymbol{F_{Oi}}$, then $\boldsymbol{F_{Oi}}$ is:

$$\boldsymbol{F}_{oi} = \delta(\boldsymbol{F}_{hi}{}^{'}\boldsymbol{W} + \boldsymbol{b}) \tag{17}$$

$$\boldsymbol{F}_{hi}{}^{'} = \boldsymbol{F}_i^{'}\boldsymbol{W}^{\boldsymbol{h}} + \boldsymbol{b}^{\boldsymbol{h}} \tag{18}$$

where

$$\begin{aligned} \mathbf{W}^{\mathbf{h}} &\in \mathbb{R}^{256 \times 32} \\ \mathbf{W} &\in \mathbb{R}^{32 \times 2} \end{aligned} \tag{19}$$

$$\begin{aligned} \boldsymbol{b}^{\boldsymbol{h}} &= \left[\boldsymbol{b}_1^{\boldsymbol{h}T}, \cdots, \boldsymbol{b}_j^{\boldsymbol{h}T}, \cdots, \boldsymbol{b}_S^{\boldsymbol{h}T}\right]^T \\ \boldsymbol{b}_1^{\boldsymbol{h}} = \boldsymbol{b}_j^{\boldsymbol{h}} &= \boldsymbol{b}_S^{\boldsymbol{h}} \in \mathbb{R}^{1 \times 32}(1 \le j \le S) \\ \boldsymbol{b} &\in \mathbb{R}^{S \times 2} \end{aligned} \tag{20}$$

where $\delta(\cdot)$ is the Softmax activation function that can be extended as:

$$\delta(z)^j = \frac{e^{z_j}}{\sum_{c=1}^{2} e^{z_c}} \tag{21}$$

The errors $\triangle\boldsymbol{E_i}$ between $\boldsymbol{F_{Ei}}$ and $\boldsymbol{F_{Oi}}$ is:

$$\triangle\boldsymbol{E}_i = -\sum \boldsymbol{F}_{Ei} ln(\boldsymbol{F}_{oi}) \tag{22}$$

The weights $\boldsymbol{W}$ and bias $\boldsymbol{b}$ are updated according to stochastic gradient descent with momentum (SGDM) algorithm:

$$\boldsymbol{W} = \theta\boldsymbol{W} + (1-\theta)\frac{\partial\triangle\boldsymbol{E}_i}{\partial\boldsymbol{W}} \tag{23}$$

$$\boldsymbol{b} = \theta\boldsymbol{b} + (1-\theta)\frac{\partial\triangle\boldsymbol{E}_i}{\partial\boldsymbol{b}} \tag{24}$$

where θ is the momentum rate. $\boldsymbol{W^h}$ and $\boldsymbol{b^h}$ can be calculated according to the chain-rule. By iteratively updating $\boldsymbol{W}$, $\boldsymbol{W^h}$, $\boldsymbol{b}$, and $\boldsymbol{b^h}$, we then have a trained ANN for our binary classification task here. Thereafter, we input each batch feature $F_i^{'}$for the classification. By aggregating all predicted categories of all batches, we then receive classification results for data in the test set. The pseudocode of our proposed framework can be found in Algorithm 4.

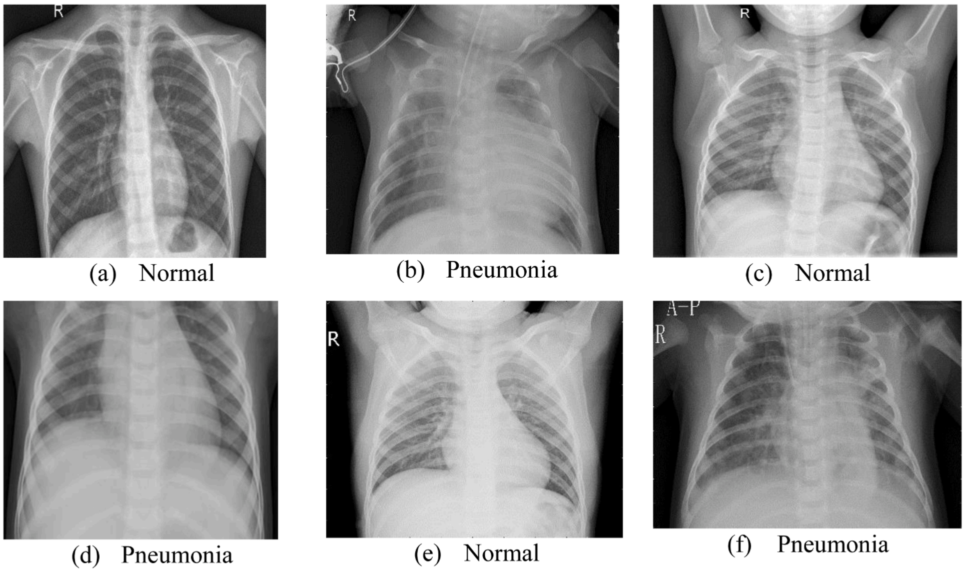

(a) Normal (b) Pneumonia (c) Normal

(d) Pneumonia (e) Normal (f) Pneumonia

Fig. 5. Samples of dataset1.

3.4. Evaluation metrics

To measure the performance of the proposed model, we use common metrics including *Sensitivity, Specificity, Accuracy, Precision* and *F1* score like many other works to measure the performance of our proposed classifier. To calculate the metrics, True Positive (***TP***), True Negative (***TN***), False Positive (***FP***) and False Negative (***FN***) are introduced.

The higher the ***TP*** and ***TN***, the better performance of classifiers that can detect true pneumonia images and normal images; The lower the ***FP*** and ***FN***, the fewer mistakes of classifiers that misclassify normal images as pneumonia images and vice versa. The sensitivity is related to ***TP*** by:

$$Sensitivity = \frac{\boldsymbol{TP}}{\boldsymbol{TP} + \boldsymbol{FN}} \tag{25}$$

The specificity, which implies the capability of classifiers on recognition of normal images, can be denoted by ***TN*** and ***FP*** by:

$$Specificity = \frac{\boldsymbol{TN}}{\boldsymbol{TN} + \boldsymbol{FP}} \tag{26}$$

The overall performance of classifiers is measured by the accuracy:

$$Accuracy = \frac{\boldsymbol{TN} + \boldsymbol{TP}}{\boldsymbol{TN} + \boldsymbol{FP} + \boldsymbol{TP} + \boldsymbol{FN}} \tag{27}$$

The *Precision* measures the percentage of real pneumonia images out of all predicted pneumonia images:

$$Precision = \frac{\boldsymbol{TP}}{\boldsymbol{TP} + \boldsymbol{FP}} \tag{28}$$

$F1$ shows the classification ability of the classifiers:

$$F1 = 2 \times \frac{Precision \times Accuracy}{Precision + Accuracy} \tag{29}$$

4. Experiment design

In this section, we will briefly go through the details about the datasets (Section 4.1) used in this research, followed by experiment settings (Section 4.2) that gives the details about the experiment configuration. The performance of the transferred networks (Section 4.3) is given before we move to the exploration of batch size *N* and the number of neighbours *k* for GNet in Section 4.4. The effectiveness of feature reconstruction and comparison of feature reconstruction methods are given in Section 4.5 and Section 4.6 respectively. We conclude this section by comparing our proposed method with the state-of-the-art methods in Section 4.7.

Table 1
Details of the dataset1.

Set	Normal	Pneumonia	Total Number
Training	1341	3875	5216
Validation	8	8	16
Testing	234	390	624
Overall	1583	4273	5856

4.1. Datasets

In this research, we validated our proposed feature reconstruction method on two public datasets from two different modalities. We used one cohort that has been confirmed with pneumonia caused by bacteria, which we named it as dataset1. In the dataset1, which is publicly available at (Chest X-Ray Images (Pneumonia) 2020), there are in total 5856 normal and pneumonia X-ray images. To provide a fair comparison platform for different systems, the training set, validation set and the test set have been partitioned beforehand. Examples of normal and pneumonia samples can be seen in Fig. 5. Details about the dataset1 are shown in Table 1.

We also examined our proposed method on another public CT-based pneumonia dataset in which the pneumonia was caused by COVID-19 and we named the dataset as dataset2 (Zhao, Zhang, He & Xie, 2020). Some sample images are shown in Fig. 6. The size of three-channel RGB images varies from 720 × 541 × 3 to 725 × 551 × 3.

Compared to images acquired through X-ray instrument, CT lung images show more advantages on image resolutions and fine-grained details. The detailed composition of dataset 2 is shown in Table 2.

4.2. Experiment settings

The configuration of this research is a personal laptop with 16 G RAM and GPU GTX1050. As we have to train transferred networks and the following ANN and GNet in a sequence, we have two different sets of parameters. Deep learning toolbox provided by Mathworks is used as the framework. For transferred networks, they are trained for 20 epochs while the initial learning rate is 10^{-4}. Batch size is 8 to prevent system crash due to the memory. We use the stochastic gradient descent with momentum (SGDM) as the optimization method. Also, we have the learning rate halved every 5 epochs to ensure the convergence. When training transferred networks with the training set, images in the training set shuffle at every epoch. Detailed settings can be seen in Table 3, which remained unchanged during the training process of networks on two datasets.

When constructing graphs for reconstruction, the size N of each batch and the number of neighbours k within each batch should be carefully chosen to make sure best performance of GNet can be achieved. When training ANN with features extracted from the transferred networks, we increased the training epochs to be 40 while other parameters have remained unchanged. We use the same parameters throughout the experiments if there are no other specifications. Then we vary N and k to explore the relationship between N, k and the performance of the ANN. Details will be presented in the following sections.

4.3. Performance of the transferred networks

To find out the best-performed state-of-the-art networks that can be transferred to our classification task here, we trained networks including AlexNet (Krizhevsky Alex, 2012), GoogLeNet (Szegedy Christian et al., 2015), SqueezeNet (Iandola et al., 2016), VGG16 (Simonyan Karen, 2014), XceptionNet (Chollet, 2017), ResNet18 (He Kaiming et al., 2016), ResNet101, InceptionV3 (Szegedy, Vanhoucke, Ioffe, Shlens & Wojna, 2016), DenseNet201 (Huang et al., 2017). All of those networks are pre-trained on ImageNet for the 1000-category classification task. To make a fair comparison amongst all of the networks, top layers including FC256, and FC2 are inserted between the Softmax layer and the dropout layer. The original Softmax layer and classification layer are, therefore, replaced by new Softmax layer and a classification layer. The numbers of learnable parameters of the networks introduced are listed in Table 4.

After training with the dataset1, the results of different networks are organized in Table 5 while ROC curves are shown in Fig. 7.

On the dataset1, strangely, XceptionNet performed best in all the transferred networks though it was not the deepest one nor newest one. The reasons why XceptionNet performed best could be two folds. One is the architectural novel of XceptionNet. In XceptionNet, shortcut connection technique, which was also being deployed in ResNet and DenseNet, is used besides depthwise separable convolution, which greatly lowers the number of training parameters in the networks. Another possible reason is the size of the input. Note that the input size of XceptionNet is 299 × 299 × 3 while the input size of other networks is no greater than 227 × 227 × 3. However, the original size of the images is greater than 1000 × 1000 × 3. Therefore, XceptionNet experienced much less information loss, which allows more representative features to be extracted. Interestingly, the performance of the networks can be even worse when the depth of networks going deeper, which also requires a longer time for training. Given this, we choose XceptionNet as our feature extractor in this classification task though the performance is still far away from satisfaction.

Similarly, we adapted and trained the same state-of-the-art networks on dataset2. The results on the validation set and the test set are shown in Tables 6 and 7 respectively. The ROC curves are shown in Fig. 8.

Both on the validation set and the test set, DenseNet201 showed the best performance amongst all the state-of-the-art networks. As can be seen from Table 4, the number of learnable parameters in DenseNet201 is not the biggest one, however, the number of layers of DenseNet201 is much greater than that of the rest of the network compared to that of the other state-of-the-art networks. Therefore,

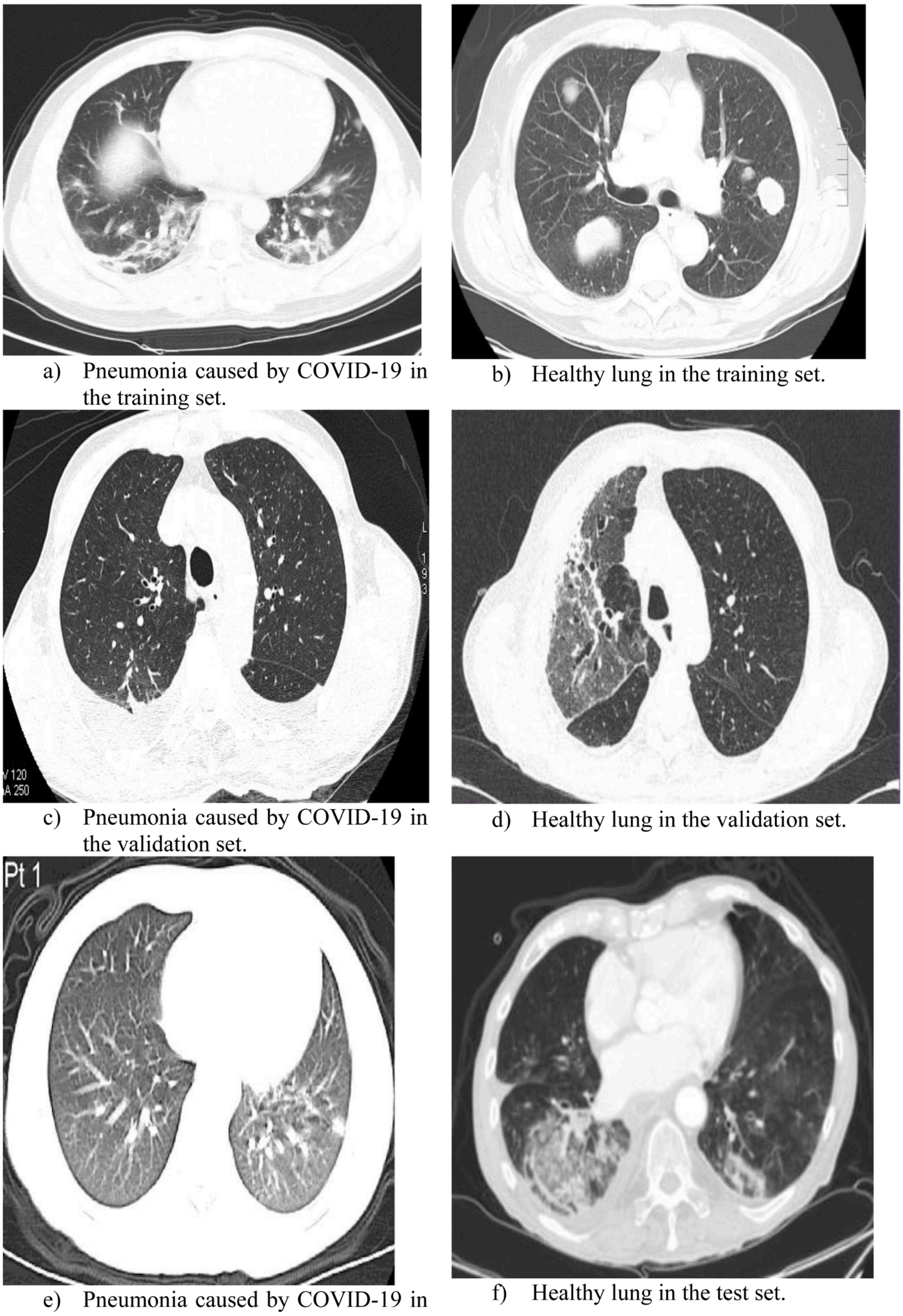

a) Pneumonia caused by COVID-19 in the training set.

b) Healthy lung in the training set.

c) Pneumonia caused by COVID-19 in the validation set.

d) Healthy lung in the validation set.

e) Pneumonia caused by COVID-19 in the test set.

f) Healthy lung in the test set.

Fig. 6. Sample images from the dataset2.

DenseNet201 could be benefited from the high density of connections between the layers, which allows more representative features to be learnt. Due to the imaging modality difference between X-ray and CT, XceptionNet, which performed best on the dataset1, turned out to have poor performance on dataset2. Therefore, we used DenseNet201 as the feature extractor when implementing GNet on dataset2.

Table 2
Details of the dataset2.

Set	Normal	Pneumonia	Total Number
Training	234	191	425
Validation	58	60	118
Testing	105	98	203
Overall	397	349	746

Table 3
Training parameters for transferred CNNs.

Parameters	Value
Maximum training epoch	20
Initial learning rate	10^{-4}
Batch size	8
Learning rate drop period	5
Learning rate drop rate	0.5
Optimization method	SGDM
Shuffle of the train set	Each epoch

Table 4
Numbers of learnable training parameter in the state-of-the-art networks.

Model name	Number of parameters(Millions)	Number of Layers
AlexNet	6.10	25
GoogLeNet	0.70	144
SqueezeNet	0.12	68
VGG16	13.84	41
XceptionNet	2.29	170
ResNet18	1.17	71
ResNet101	4.45	347
DenseNet201	1.98	708

Table 5
Performance of state-of-the-art networks on the dataset1.

Model name	Specificity	Sensitivity	F1	Precision	AUC	Accuracy
AlexNet	0.9974	0.5000	0.6648	0.9915	0.9747	0.8109
GoogLeNet	0.9949	0.4744	0.6398	0.9823	0.9680	0..7997
SqueezeNet	0.9974	0.4402	0.6095	0.9904	0.9730	0.7885
VGG16	1.0000	0.3462	0.5143	1.0000	0.9627	0.7548
XceptionNet	0.9872	0.6453	**0.7744**	0.9679	0.9539	**0.8590**
ResNet18	0.9974	0.5598	0.7158	0.9924	**0.9788**	0.8333
ResNet101	**1.0000**	0.5385	0.7000	**1.0000**	0.9674	0.8269
DenseNet201	**1.0000**	0.4487	0.6195	**1.0000**	0.9705	0.7933

4.4. The influence of batch size N and number of neighbours k

For dataset1, after extracting features by XceptionNet, we then reconstruct features according to generated graphs. However, the batch size *N* of features and the number *k* of neighbours being considered are two parameters that are related to the performance of the proposed GNet. Therefore, we explored different sets of *N* and *k* to optimize the performance of GNet. In Table 8, we show a result of GNet when *N* is 32 while *k* varies from 4 to 28. In Fig. 9, the ROC curves of GNet with different configurations are shown. As can be seen, all of the GNets showed an AUC over 0.96 with high AUC at 0.99 achieved. Interestingly, the performance of GNet when *k* equals to 24 seems to be saturated to that of GNet when *k* equals to 28

From Table 8, we can conclude that the performance of GNet increases along with the increment of neighbours considered. To explore the influence of batch size *N* to the performance of GNet, we examined the performance when *N* is 64, 96, 128 and 156 while *k* keeps varying. From Tables 9, Table 10, Table 11, and 12, we showed the performance of GNet when *N* is 64, 96, 128 and 156 respectively. The corresponding ROC curves are shown in Figs. 10–13 respectively.

A graph that showed the relationship between batch size *N* and the number of neighbours *k* on dataset1 is given in Fig. 14. As can be seen from Fig. 14, the accuracy increases along with the *k* when *N* is small. However, the accuracy seems to be saturated when *N* is relatively large though *k* increases. However, it is noticeable that the accuracy imrpoves along with the increament of *k*/*N* rate.

Following a similar pattern, we choose the trained networks that showed the best performance on the dataset2, which was

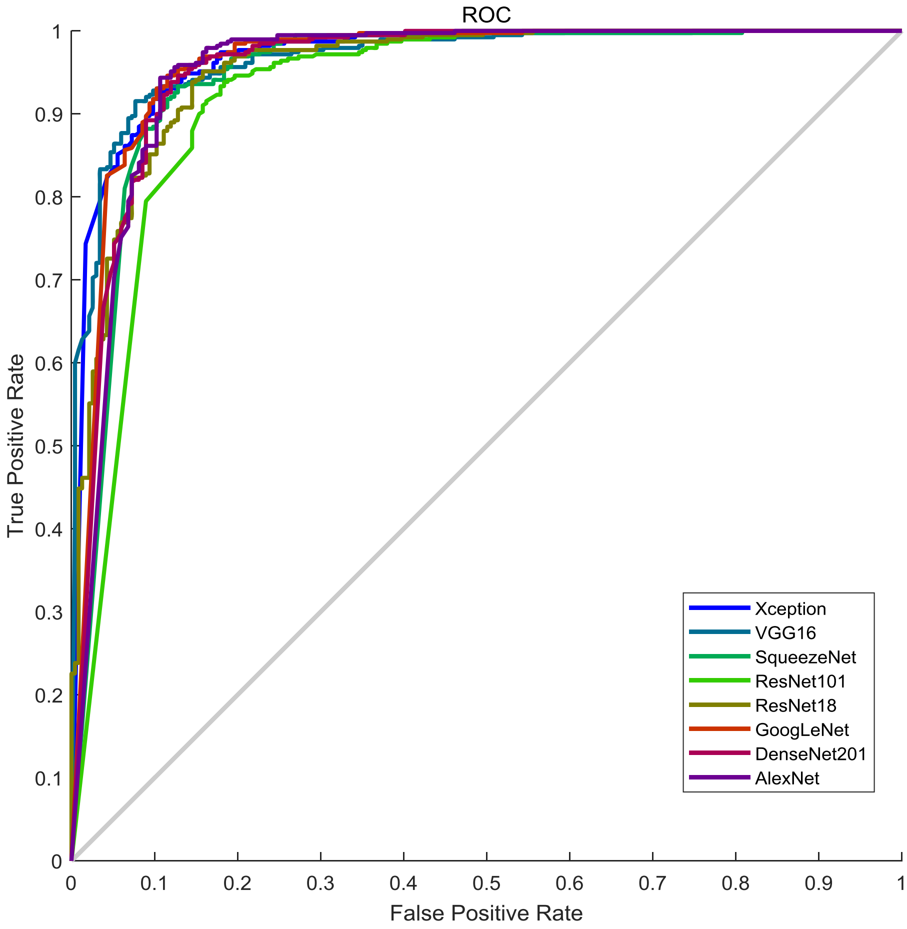

Fig. 7. ROC curves of the state-of-the-art networks on the test set of dataset1.

Table 6

Performance of the state-of-the-art networks on the validation set of dataset2.

Model name	Specificity	Sensitivity	F1	Precision	AUC	Accuracy
AlexNet	0.7586	**0.7333**	0.7458	0.7586	0.7957	0.7458
GoogLeNet	0.6552	0.4667	0.5185	0.5833	0.6293	0.5593
SqueezeNet	0.5517	0.7167	0.6667	0.6232	0.6293	0.6356
VGG16	0.6724	0.7500	0.7258	0.7031	0.7888	0.7119
XceptionNet	0.6897	0.6333	0.6552	0.6786	0.6718	0.6610
ResNet18	0.7069	**0.7333**	0.7273	0.7213	0.8491	0.7203
ResNet101	0.7759	0.6167	0.6727	0.7400	0.7787	0.6949
DenseNet201	**0.8276**	0.7000	**0.7500**	**0.8077**	**0.8678**	**0.7627**

Table 7

Performance of the state-of-the-art networks on the test set of dataset2.

Model name	Specificity	Sensitivity	F1	Precision	AUC	Accuracy
AlexNet	0.7429	0.6735	0.6911	0.7097	0.7920	0.7094
GoogLeNet	0.7619	0.6837	0.7053	0.7283	0.7913	0.7241
SqueezeNet	0.7143	0.6531	0.6667	0.6809	0.6909	0.6847
VGG16	0.8095	0.6939	0.7312	0.7727	0.8331	0.7537
XceptionNet	0.6381	**0.7041**	0.6732	0.6449	0.7030	0.6700
ResNet18	0.7619	0.6837	0.7053	0.7283	0.7883	0.7241
ResNet101	0.7714	0.6429	0.6811	0.7241	0.7749	0.7094
DenseNet201	**0.8571**	0.6735	**0.7374**	**0.8148**	**0.8597**	**0.7685**

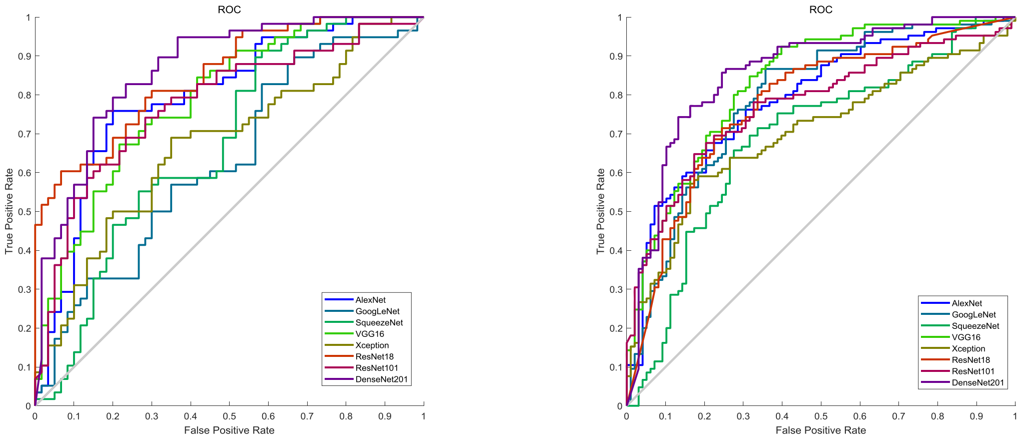

a) ROC curves of the state-of-the-art networks on the validation set of dataset2.

b) ROC curves of the state-of-the-art networks on the test set of dataset2.

Fig. 8. ROC curves on dataset2.

Table 8
Performance of GNet on the dataset1 when $N = 32$ and $k = 4$, 8, 12, 16, 24, 28.

k	Specificity	Sensitivity	F1	Precision	AUC	Accuracy
4	**1.0000**	0.4701	0.6395	**1.0000**	0.9602	0.8013
8	**1.0000**	0.7650	0.8668	**1.0000**	0.9892	0.9119
12	**1.0000**	0.5812	0.7351	**1.0000**	0.9925	0.8429
16	0.9949	**0.9231**	**0.9558**	0.9908	0.9977	**0.9679**
24	**1.0000**	0.9103	0.9530	**1.0000**	**0.9999**	0.9663
28	**1.0000**	0.9103	0.9530	**1.0000**	**0.9999**	0.9663

DenseNet201 in this scenario, as the feature extractor. We then vary k and N to specify the best configuration of the proposed GNet, where $N \in [32,\ 64,\ 96]$, k increases from one-quarter of N to the number close to N by an integer multiple of 4. Table 13 and Table 14 showed the results of GNet on the validation set and the test set of dataset2 when $N = 32$ respectively. The ROC curves are shown in Fig. 15.

We also evaluated the performance of GNet when N is 64 while k varies from 8 to 56 by integer multiples of 4. Details about the results on the validation set and the test set of dataset2 can be seen in Tables 15 and 16 while ROC curves are shown in Fig. 16.

Due to the limited number of images in the validation set on dataset2, the maximum N is chosen to be 96 instead of 128 on dataset1. The detailed results of GNet on the validation set and the test set when $N = 96$ are shown in Tables 17 and 18 while the corresponding ROC curves are shown in Fig. 17.

Similarly, we drew graphs that represent the relationship between the performance and k/N rate on the validation set and the test set of dataset2 as can be seen in Fig. 18.

As can be seen, the best configuration of GNet on the validation set and the test set are quite different. The performance of GNet fluctuates when k and N are not optimal. Also, due to the limited number of images, a greater number of N doesn't guarantee high performance. However, a rough conclusion can be drawn from Fig. 18 is that when k/N is greater than or close to 0.8 an overall higher performance can be found. A similar conclusion can be found in Fig. 14.

4.5. *Effectiveness of feature reconstruction*

To evaluate the performance of the proposed method on the detection of pneumonia, we then directly trained XceptionNet with the dataset1 and used the trained XceptionNet as the feature extractor. ANN with the same structure as our GNet is used as the classifier. To validate the effectiveness of feature reconstruction on dataset1, we also examined the performance of ANN when the input is originally extracted features by XceptionNet. Besides, SVM and Decision Tree, two classical supervised classifiers, have been introduced to make comparisons with our proposed model. To avoid confusion, we name ANN trained by original features as ANN$_{raw}$. Two networks are trained with the same training parameters. The classification results of the two trained networks are given in Table 19.

Parameters in the parenthesis mean the given parameters are used to train GNet. As can be seen, the networks GNet trained with reconstructed features performed much better than the network trained with original features extracted by XceptionNet. Though batch size N and k varies, the accuracy showed a consistent gain compared to the results given by ANN$_{raw}$. When it comes to computational

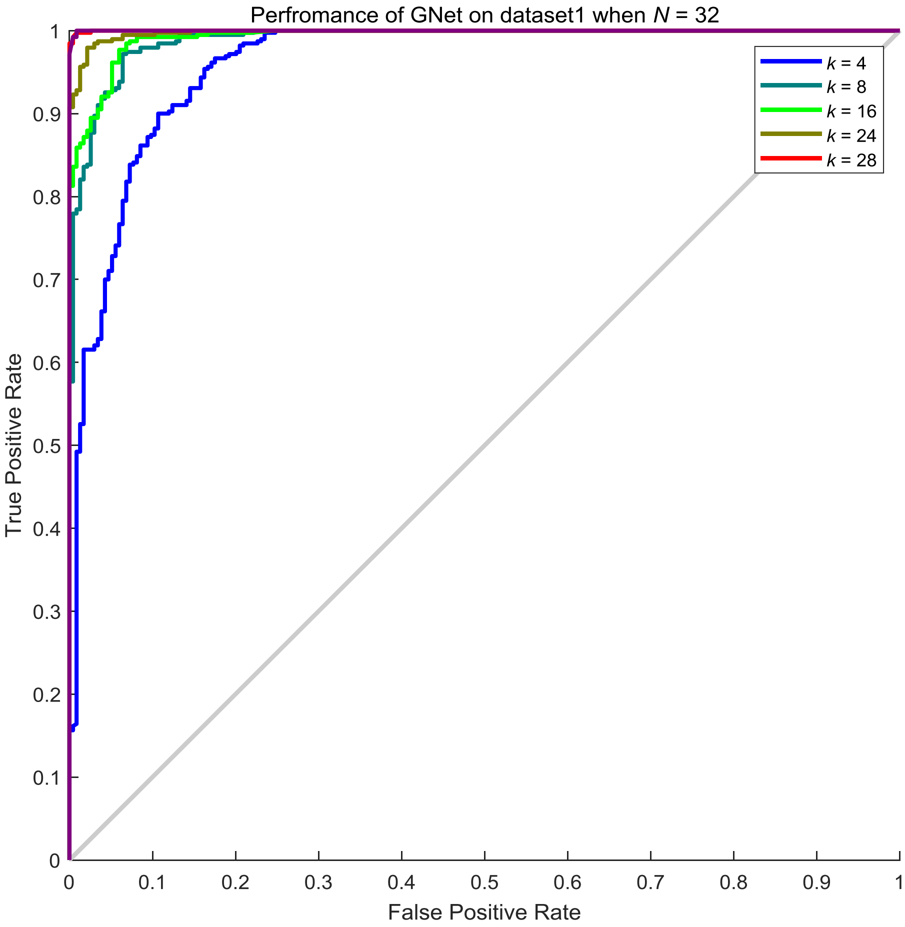

Fig. 9. ROC curves of GNet on the test set of dataset1 when $N = 32$.

Table 9
Performance of GNet on the test set of dataset1 when $N = 64$ and $k = 8, 16, 24, 28, 32, 48, 56$.

k	Specificity	Sensitivity	F1	Precision	AUC	Accuracy
8	**1.0000**	0.6325	0.7749	**1.0000**	0.9837	0.8622
16	**1.0000**	0.4487	0.6195	**1.0000**	0.9872	0.7933
24	0.9923	0.8205	0.8951	0.9846	0.9978	0.9279
28	0.9974	0.7735	0.8702	0.9945	0.9979	0.9135
32	0.9974	0.7735	0.8702	0.9945	0.9979	0.9135
48	0.9872	**0.9744**	**0.9764**	0.9785	0.9985	**0.9824**
56	0.9436	**1.0000**	0.9551	0.9141	**0.9998**	0.9647

Table 10
Performance of GNet on the test set of dataset1 when $N = 96$ and $k = 12, 24, 36, 48, 60, 72, 84$.

k	Specificity	Sensitivity	F1	Precision	AUC	Accuracy
12	0.9974	0.6795	0.8071	0.9938	0.9842	0.8782
24	**1.0000**	0.4615	0.6316	**1.0000**	0.9793	0.7981
36	0.9974	0.7094	0.8279	0.9940	0.9932	0.8894
48	0.9846	0.8462	0.9041	0.9706	0.9936	0.9327
60	**1.0000**	0.6923	0.8182	**1.0000**	0.9964	0.8846
72	**1.0000**	0.7179	0.8358	**1.0000**	0.9974	0.8942
84	0.9487	**1.0000**	**0.9590**	0.9213	**0.9985**	**0.9679**

Table 11
Performance of GNet on the test set of dataset1 when $N = 128$ and $k = 16, 32, 48, 64, 80, 96, 112$.

k	Specificity	Sensitivity	F1	Precision	AUC	Accuracy
16	**1.0000**	0.5385	0.7000	**1.0000**	0.9911	0.8269
32	**1.0000**	0.4573	0.6276	**1.0000**	0.9898	0.7965
48	0.9949	0.8376	0.9074	0.9899	0.9976	0.9359
64	0.9897	0.9487	0.9652	0.9823	0.9987	0.9744
80	0.9846	0.9872	0.9809	0.9747	0.9987	0.9856
96	0.9795	**1.0000**	**0.9872**	0.9669	**0.9989**	**0.9872**
112	0.9436	**1.0000**	0.9551	0.9141	**0.9989**	0.9647

Table 12
Performance of GNet on the test set of dataset1 when $N = 156$ and $k = 16, 32, 48, 64, 80, 96, 112, 128, 144$.

k	Specificity	Sensitivity	F1	Precision	AUC	Accuracy
16	0.9974	0.6325	0.7728	**0.9933**	0.9795	0.8606
32	0.9949	0.7179	0.8317	0.9882	0.9892	0.8910
48	**0.9974**	0.5256	0.6872	0.9919	0.9910	0.8205
64	0.9923	0.8034	0.8847	0.9843	0.9915	0.9215
80	0.9692	0.9402	0.9442	0.9483	0.9924	0.9583
96	0.9462	0.9915	**0.9631**	0.9170	0.9939	**0.9631**
112	0.9282	**1.0000**	0.9435	0.8931	0.9969	0.9551
128	0.8974	**1.0000**	0.9213	0.8540	**0.9971**	0.9359
144	0.9256	**1.0000**	0.9416	0.8897	0.9969	0.9535

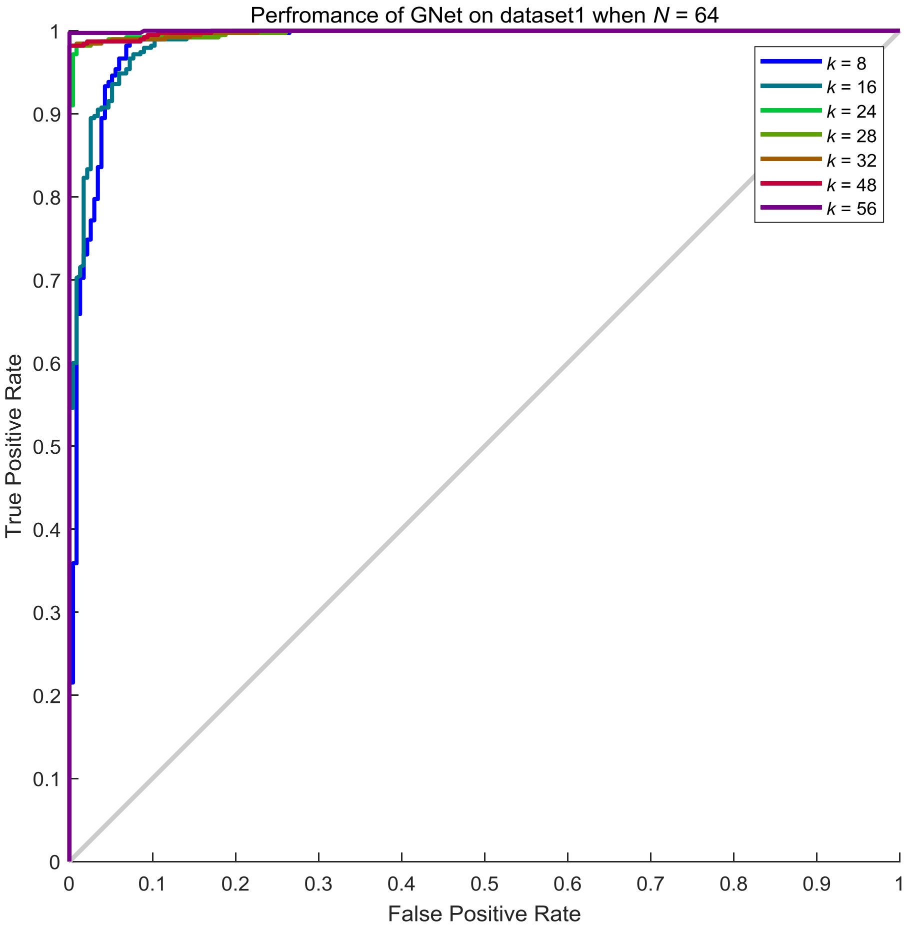

Fig. 10. ROC curves of GNet on the test set of dataset1 when $N = 64$.

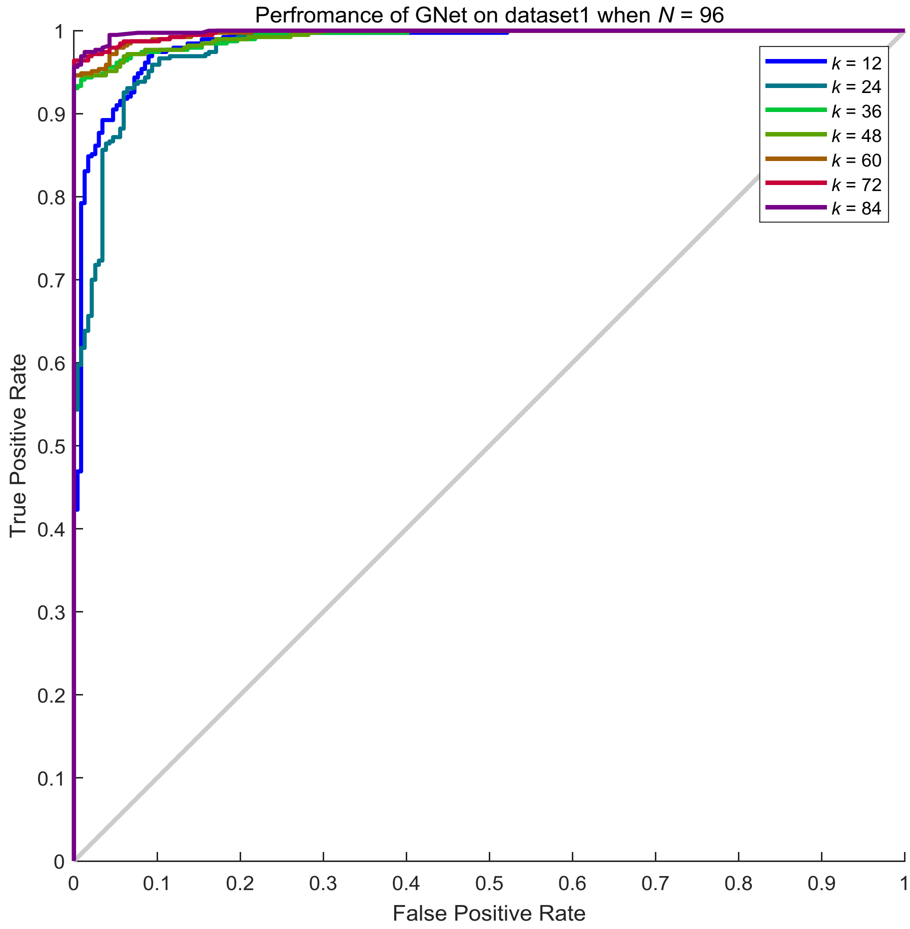

Fig. 11. ROC curves of GNet on the test set of dataset1 when $N = 96$.

costs on training two networks, our GNet takes a longer time because of graph construction and graph-feature combination process during feature reconstruction. However, our proposed GNet becomes more advantageous in the prediction phase as the network allows simultaneous classification for multiple images. Considering the computational capability of our laptop, the cost is still expedient. Therefore, we believe the proposed feature reconstruction method will be transplantable to other machines as well. Therefore, we believe our reconstruction method is effective to improve the performance of ANN.

On dataset2, DenseNet201 showed the best performance amongst all of the state-of-the-art networks. Hence, the input of ANN and GNet thereby are the features extracted by DenseNet201.The same architecture of ANN and GNet is employed when making the comparison. As can be seen in Table 20, the performance of GNet is significantly higher than ANN and SVM.

4.6. Comparison of feature reconstruction methods

In this section, we compared our proposed feature reconstruction method with PCA-based feature reconstruction method. The eigenvalues and eigenvectors are calculated and selected in an descending order. For two datasets, we ensure that the selected components are able to explain more than 98% of all variability. Therefore, the dimensions of features from two datasets have been reduced from 256 to 152 and 131 respectively. We then trained classifiers including ANN, SVM and decision tree based on the features reconstructed by PCA. Also, we recontructed the features from two datasets based on our graph-knowledge reconstruction method. For simplicity, we choose N to be 32 while k remains to be 16.

As can be seen from Tables 19 and 21, the performance of ANN decreased slightly while the performance of SVM and decision tree increases. A contradictory conclusion can be drawn from Table 22 that SVM and decision tree performed even worse while the performance of ANN has been improved significantly. Therefore, we may roughly conclude that both PCA-based reconstruction method and our method failed to significantly improve the performance of SVM and decision tree but our method indeed improves the specificity to 1.

On dataset2, we just repeated the same procedures and presented the results in Tables 23 and 24 respectively. Note that the size of the input of ANN has been adjusted to 131 correspondingly. As can be seen, the performance of SVM remains unchanged when PCA is used while our method harmed the performance of SVM. For the decision tree, both methods improved the performance of the decision

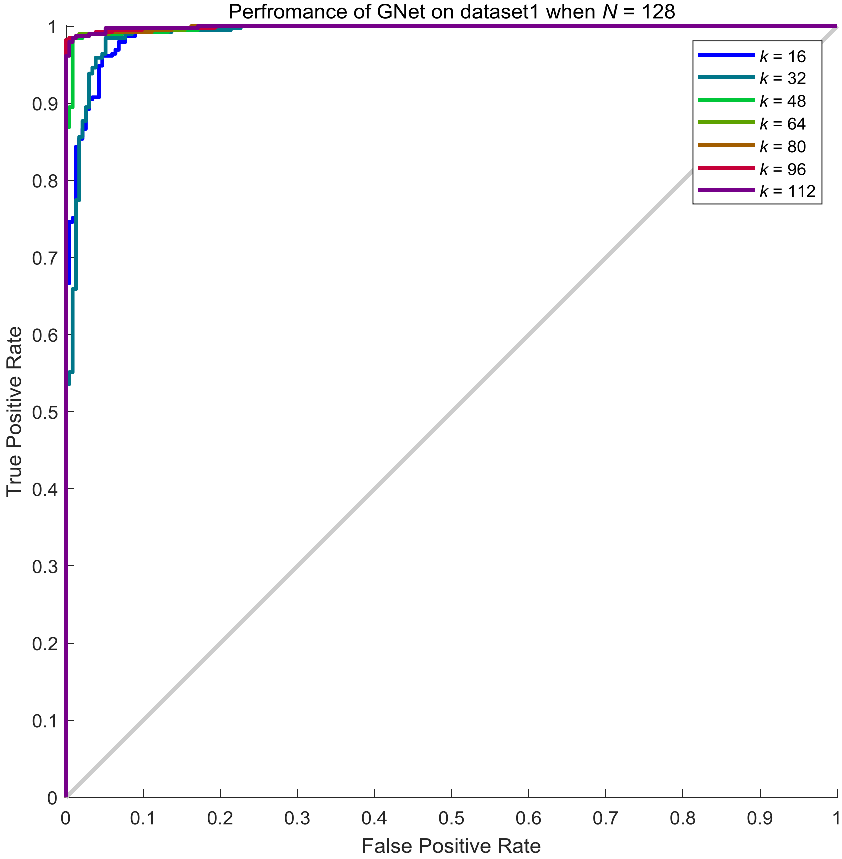

Fig. 12. ROC curves of GNet on the test set of dataset1 when $N = 128$.

tree. Based on the results from two datasets, we are convinced that our feature reconstruction method shows great advantage on the improving the performance of ANN while how to improve the performance of SVM and decision tree by our method remains to be explored.

4.7. Comparison of state-of-the-art methods

Considerable works are focusing on designing high accuracy systems for the detection of pneumonia. To provide a fair comparison, we compared our method to methods that have been validated on the same datasets. For pneumonia caused by common bacteria and virus, the performance of different methods is shown in Table 25.

Sensitivity measures the ability of proposed methods on making correct diagnostic results on sick people as patients. Compared to high specificity, **high sensitivity is of even greater significance,** because healthy people misdiagnosed as the sick suffers much lower risk than patients misdiagnosed as healthy people. As can be seen, our method surpassed the majority of the state-of-the-art methods while our method achieved the highest sensitivity, which means our method shows the stronger capability of detecting pneumonia images.

(The higher the sensitivity the better performance of the proposed methods on detecting real pneumonia images)

To provide a fair comparison with methods based on chest CT images, we also compared our method with the state-of-the-art methods. Detailed results can be seen in Table 26.

(The higher the sensitivity the better performance of the proposed methods on detecting real pneumonia images)

5. Discussion

In this paper, we proposed a novel classifier for the detection of pneumonia based on X-ray and CT images. The proposed feature reconstruction method greatly improved the performance of the neural network with simple architectures. Before inputting images to all models, preprocessing methods are applied to adapt the images for the models. As the sizes of images in the dataset may vary, images are resized for different networks to meet the size requirement of input. Also, the images are not squared while the original height and width of images are greater than 1000 pixels. Therefore, distortion may be introduced due to image resizing. Though XceptionNet performed best amongst all CNNs when dataset1 was concerned, it is, however, could be the larger input images that

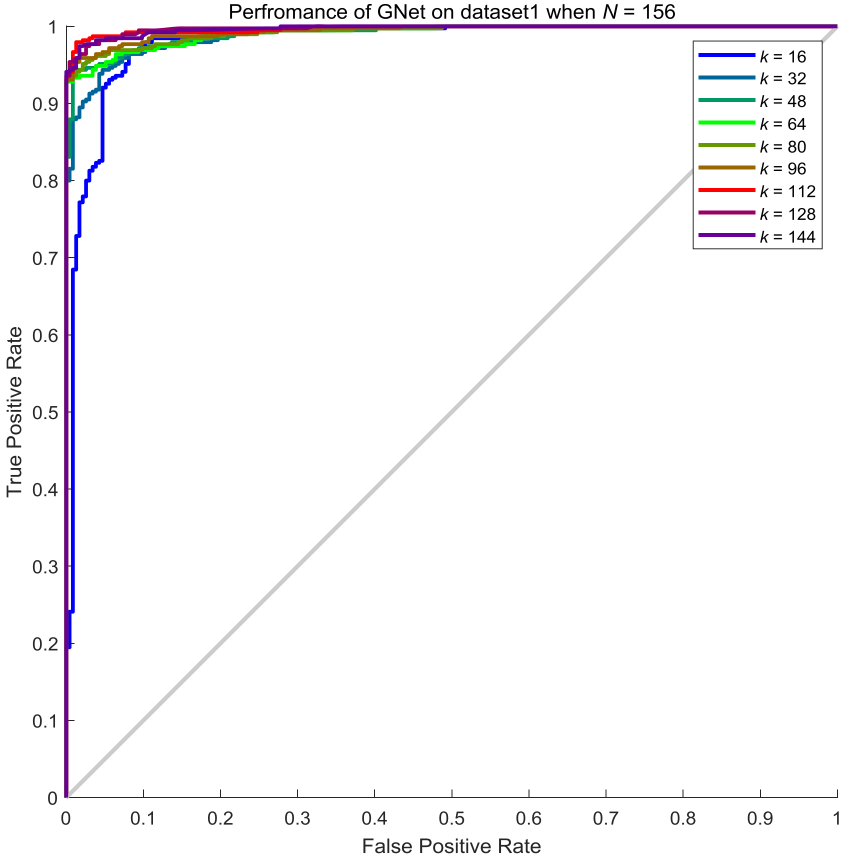

Fig. 13. ROC curves of GNet on the test set of dataset1 when $N = 156$.

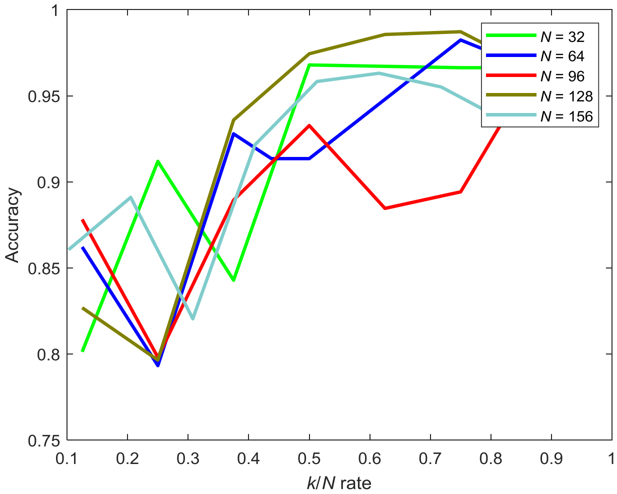

Fig. 14. The relationship between k/N and accuracy on dataset1. (k/N means the ratio between the number of neighbours and batch size N.).

allow more features to be extracted. In datatset1, images are one-channel grey-scale images. Consequently, images in datasets are converted to three-channel RGB images. For CT-based images in dataset2, DenseNet201, which could be benefited from the rich connections between layers, showed the best performance amongst all of the networks. Except for the procedures mentioned above, no other data augmentation methods are involved. As for similarity measurement in the graph generation process, many other methods can be applied. However, Euclidean distance is the most straightforward way to quantify the difference between features. When reconstructing features, the feature to be reconstructed can be reconstructed by the top k nearest neighbours found. However, the

Table 13
Performance of GNet on the validation set of dataset2 when $N = 32$ and $k = 4, 8, 16, 20, 24, 28$.

k	Specificity	Sensitivity	F1	Precision	AUC	Accuracy
4	0.6724	0.8833	0.8030	0.7361	0.8744	0.7797
8	0.8966	0.7833	0.8319	0.8868	0.9080	0.8390
16	0.8793	**1.0000**	**0.9449**	0.8955	**0.9980**	**0.9407**
20	**1.0000**	0.75000	0.8571	1.0000	0.9862	0.8729
24	0.6724	**1.0000**	0.8633	0.7595	0.9971	0.8390
28	0.5862	**1.0000**	0.8333	**0.7143**	**0.9980**	0.7966

Table 14
Performance of GNet on the test set of dataset2 when $N = 32$ and $k = 4, 8, 16, 20, 24, 28$.

k	Specificity	Sensitivity	F1	Precision	AUC	Accuracy
4	0.8190	0.8980	0.8585	0.8224	0.9115	0.8571
8	0.9810	0.8367	0.9011	0.9762	0.9709	0.9113
16	0.9810	0.9286	0.9529	0.9785	0.9805	0.9557
20	**1.0000**	0.8776	0.9348	**1.0000**	**0.9862**	0.9409
24	0.7905	**0.9796**	0.8889	0.8136	0.9853	0.8818
28	**0.9810**	**0.9796**	**0.9796**	0.9796	0.9850	**0.9803**

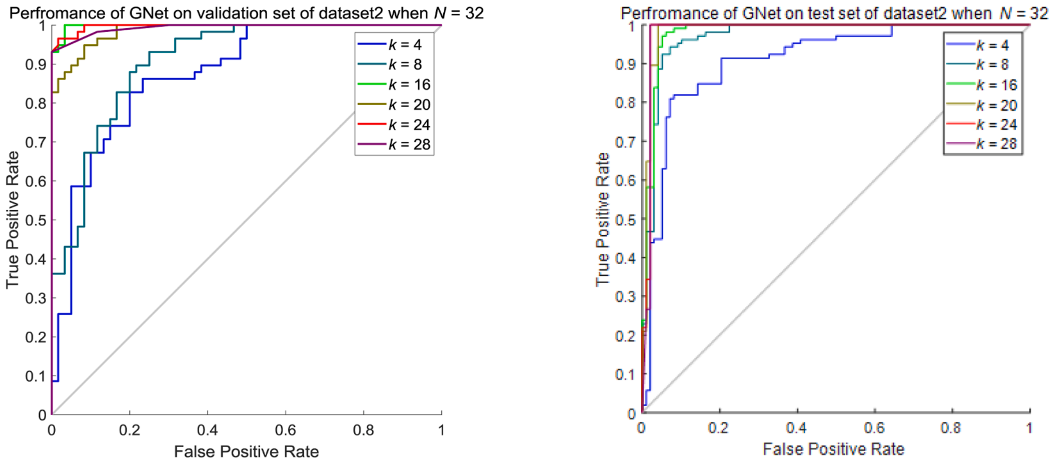

ROC curves of GNet on the validation set of dataset2 when $N = 32$.

ROC curves of GNet on the test set of dataset2 when $N = 32$.

Fig. 15. Performance of GNet on dataset2 when $N = 32$.

performance of reconstruction could be significantly affected by the distribution of features in the same batch. Therefore, we choose to include the original feature as one of the top k nearest neighbours and therefore mitigate the influence brought by distributions of features. Graph construction and graph-feature combination are the two most important procedures during the process of feature reconstruction. However, these two procedures bring no significant computational costs both in training and prediction period. In general, the validation set is used to validate the performance of the proposed classifiers. However, the validation set in the dataset involved is too small to act as a useful validation set. Therefore, the dataset is suggested to repartition to form real useful validation set.

6. Conclusion

In this paper, we proposed a novel deep learning model for the detection of pneumonia by integrating graph knowledge for feature reconstruction. We hypothesise that features will be more representative if they are reconstructed by neighbours. Based on this, we proposed a graph-based reconstruction method, which turns out to be simple yet effective. If we consider the reconstruction as a component in the following GNet, then the proposed GNet turns into a simple graph neural network with only one layer. Experiments on a large dataset showed the high performance of the proposed feature reconstruction method and the proposed model, whose performance surpassed the state-of-the-art methods. The conclusion is also supported by the results on a public COVID-19 CT-image dataset, where we achieved 99% accuracy.

However, some limitations of this research remain and will be listed as our future work. The sizes of datasets are still very small to

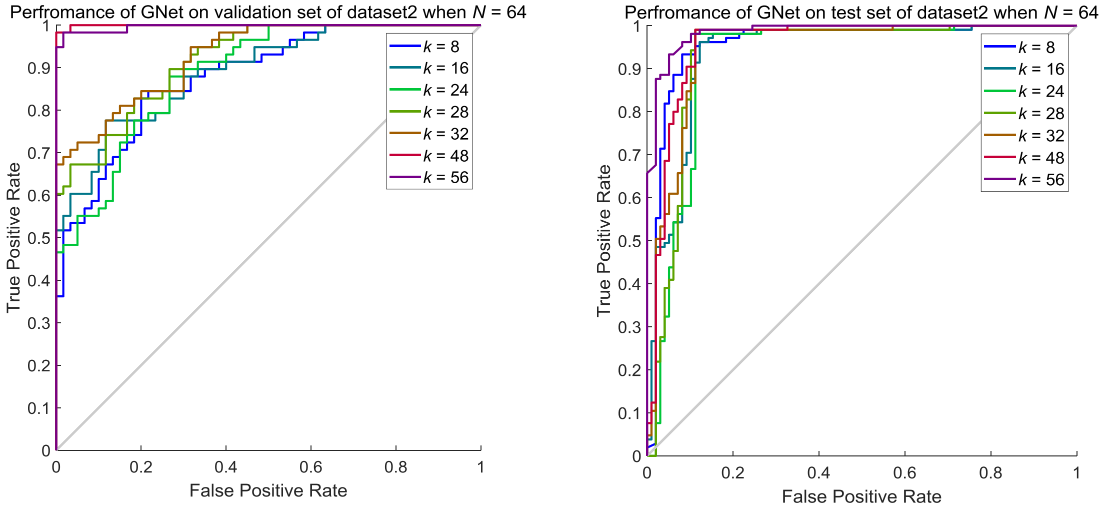

a) ROC curves of GNet on the validation set of dataset2 when $N = 64$.

b) ROC curves of GNet on the test set of dataset2 when $N = 64$.

Fig. 16. Performance of GNet on dataset2 when $N = 64$.

Table 15

Performance of GNet on the validation set of dataset2 when $N = 64$ and $k = 8, 16, 24, 28, 32, 48, 56$.

k	Specificity	Sensitivity	F1	Precision	AUC	Accuracy
8	0.9138	0.5833	0.7000	0.8750	0.8805	0.7458
16	0.7759	0.8833	0.8413	0.8030	0.8914	0.8305
24	0.9655	0.5667	0.7083	0.9444	0.8874	0.7627
28	0.7759	0.8333	0.8130	0.7937	0.9190	0.8051
32	0.6897	0.9667	0.8529	0.7632	0.9287	0.8305
48	0.9310	**1.0000**	**0.9677**	0.9375	**0.9994**	**0.9661**
56	**0.9828**	0.9000	0.9391	**0.9818**	0.9966	0.9407

Table 16

Performance of GNet on the test set of dataset2 when $N = 64$ and $k = 8, 16, 24, 28, 32, 48, 56$.

k	Specificity	Sensitivity	F1	Precision	AUC	Accuracy
8	0.9905	0.6122	0.7547	0.9836	0.9560	0.8079
16	0.9619	0.8571	0.9032	0.9545	0.9365	0.9113
24	0.9905	0.6633	0.7927	0.9848	0.9218	0.8325
28	0.9905	0.8776	0.9297	0.9885	0.9325	0.9360
32	0.9810	**0.8878**	**0.9305**	0.9775	0.9457	**0.9360**
48	0.9905	0.8367	0.9061	0.9880	**0.9565**	0.9163
56	**1.0000**	0.6531	0.7901	**1.0000**	**0.9565**	0.8325

Table 17

Performance of GNet on the validation set of dataset2 when $N = 96$ and $k = 12, 16, 24, 32, 48, 64, 80$.

k	Specificity	Sensitivity	F1	Precision	AUC	Accuracy
12	0.8276	0.7000	0.7500	0.8077	0.8236	0.7627
16	0.7414	0.6667	0.6957	0.7273	0.8336	**0.7934**
24	0.7586	0.5500	0.6168	0.7021	0.7667	0.6525
32	0.7586	0.6833	0.7130	0.7455	0.8034	0.7203
48	0.7241	0.6822	0.7009	0.7193	0.8167	0.7034
64	0.4138	**0.9667**	**0.7632**	0.6304	0.8037	0.6949
80	**0.8621**	0.6167	0.7048	**0.8222**	**0.8609**	0.7373

Table 18
Performance of GNet on the test set of dataset2 when $N = 96$ and $k = 12$, 16, 24, 28, 32, 48, 64, 80.

k	Specificity	Sensitivity	F1	Precision	AUC	Accuracy
12	0.9810	0.8469	0.9071	0.9765	0.9680	0.9163
16	0.9524	0.7347	0.8229	0.9351	0.9352	0.8473
24	0.9810	0.7653	0.8571	0.9740	0.9736	0.8768
32	0.9810	0.9184	0.9474	0.9783	0.9857	0.9507
48	1.0000	0.8878	0.9405	1.0000	**0.9979**	0.9458
64	0.9333	**0.9898**	0.9604	0.9327	0.9935	0.9606
80	**1.0000**	0.9796	**0.9897**	**1.0000**	0.9948	**0.9901**

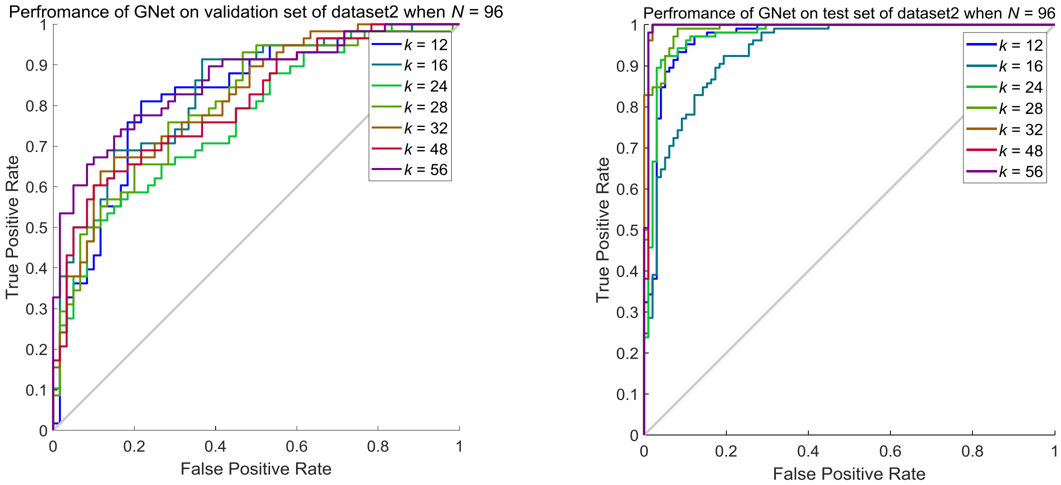

a) ROC curves of GNet on the validation set of dataset2 when $N = 96$.

b) ROC curves of GNet on the test set of dataset2 when $N = 96$.

Fig. 17. Performance of GNet on dataset2 when $N = 96$.

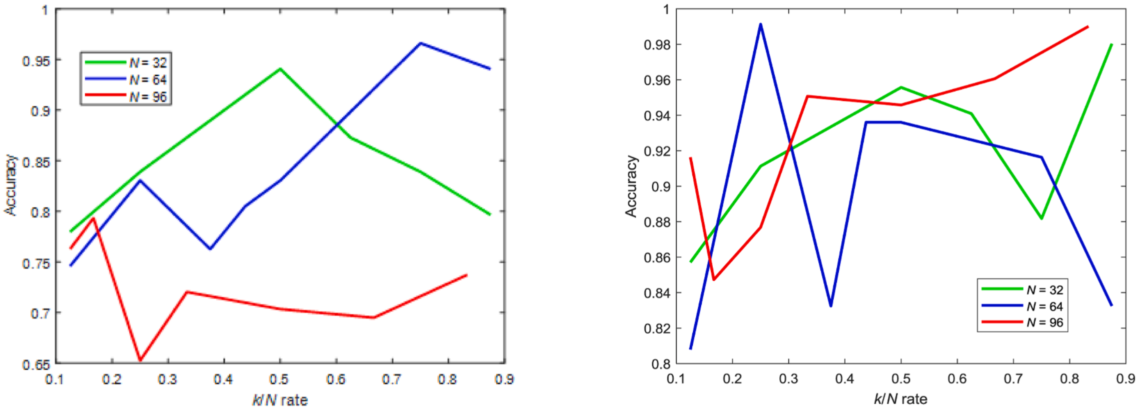

a) k/N rate on the validation set of dataset2

b) k/N rate on the test set of dataset2

Fig. 18. The relationship between k/N rate and Accuracy on dataset2.

produce more convincing results. The construction of the graph and the reconstruction of features are vital parts of our methods. However, there are also more details remain to be explored. For example, we chose a batch size N that is smaller than the dimensions of the input of ANN throughout all the experiments. What if we choose an even larger N that is greater than the dimension of the input? Also, the design of transitional fully connected layers and optimization of the ANN architecture remains to be further explored. However, ANN showed higher priority to other classifiers such as SVM and decision tree. Nevertheless, these details will be implemented in our future work.

Table 19
Performance of networks feed with different features on dataset1.

Model name	Specificity	Sensitivity	F1	Precision	Accuracy
ANN$_{raw}$	0.9385	0.7949	0.8378	0.8857	0.8846
SVM	0.9821	0.5897	0.7282	0.9517	0.8349
Decision Tree	0.9769	0.5470	0.6900	0.9343	0.8157
GNet ($N = 32$, $k = 16$)	**0.9949**	0.9231	0.9558	**0.9908**	0.9679
GNet ($N = 64$, $k = 48$)	0.9872	0.9744	0.9764	0.9785	0.9824
GNet ($N = 96$, $k = 84$)	0.9487	**1.0000**	0.9590	0.9213	0.9679
GNet ($N = 128$, $k = 96$)	0.9846	0.9915	**0.9831**	0.9748	**0.9872**
GNet ($N = 156$, $k = 96$)	0.9462	0.9915	0.9631	0.9170	0.9631

Table 20
Performance of networks feed with different features on the test set of dataset2.

Model name	Specificity	Sensitivity	F1	Precision	Accuracy
ANN$_{raw}$	0.7810	0.6633	0.6989	0.7386	0.7241
SVM	0.8857	0.7347	0.7912	0.8571	0.8128
Decision Tree	0.8286	0.6224	0.6893	0.7722	0.7291
GNet ($N = 32$, $k = 28$)	0.9810	**0.9796**	**0.9796**	0.9796	0.9803
GNet ($N = 64$, $k = 28$)	0.9905	0.8776	0.9297	0.9885	0.9360
GNet ($N = 96$, $k = 80$)	**1.0000**	**0.9796**	**0.9897**	**1.0000**	**0.9901**

Table 21
Performance of classifiers when input is reconstructed by PCA on the test set of dataset1.

Model name	Specificity	Sensitivity	F1	Precision	Accuracy
ANN	0.9385	**0.7778**	**0.8273**	0.8835	**0.8782**
SVM	0.9821	0.5940	0.7316	0.9521	0.8365
Decision Tree	**0.9846**	0.6026	0.7402	**0.9592**	0.8413

Table 22
Performance of classifiers when input is reconstructed by our method on the test set of dataset1.

Model name	Specificity	Sensitivity	F1	Precision	Accuracy
ANN	0.9949	**0.9231**	**0.9558**	0.9908	**0.9679**
SVM	**1.0000**	0.5427	0.7036	**1.0000**	0.8285
Decision Tree	**1.0000**	0.4701	0.6395	**1.0000**	0.8013

Table 23
Performance of classifiers when input is reconstructed by PCA on the test set of dataset2.

Model name	Specificity	Sensitivity	F1	Precision	Accuracy
ANN	0.8095	0.5510	0.6279	0.7297	0.6847
SVM	0.8857	**0.7347**	**0.7912**	0.8571	**0.8128**
Decision Tree	**0.9333**	0.5816	0.7037	**0.8906**	0.7635

Table 24
Performance of classifiers when input is reconstructed by our method on the test set of dataset2.

Model name	Specificity	Sensitivity	F1	Precision	Accuracy
ANN	0.9810	**0.9286**	**0.9529**	0.9785	**0.9557**
SVM	**1.0000**	0.2347	0.3802	**1.0000**	0.6305
Decision Tree	0.9429	0.6122	0.7317	0.9091	0.7833

CRediT authorship contribution statement

Xiang Yu: Conceptualization, Methodology, Software, Validation, Data curation. **Shui-Hua Wang:** Resources, Investigation, Project administration, Funding acquisition. **Yu-Dong Zhang:** Resources, Formal analysis, Investigation, Data curation, Writing - review & editing, Supervision, Project administration, Funding acquisition.

Table 25
Methods of pneumonia detection.

Model name	Specificity	Sensitivity	Precision	Accuracy
Liang (Liang & Zheng, 2019)	0.9549	0.9670	0.8910	0.9050
Wang[22](Wang and Xia 2018)	0.9949	0.9017	0.9906	0.9599
Rajourkar[3](Rajpurkar, Irvin et al. 2017)	0.9795	0.9359	0.9648	0.9631
Kermany[42] Kermany et al., 2018	0.9872	0.9615	0.9783	0.9776
Islam[4](Islam, Wijewickrema et al.)	**0.9918**	0.9880	**0.9918**	**0.9899**
Ours method	0.9846	**0.9915**	0.9748	0.9872

Table 26
Methods of pneumonia detection caused by COVID-19.

Model name	Specificity	Sensitivity	Precision	Accuracy
Zhao (Zhao et al., 2020)	–	–	–	0.89
Wu (Wu et al., 2020)	0.93	0.95	–	0.93
Jaiswal (Jaiswal, Gianchandani, Singh, Kumar & Kaur, 2020)	0.96	–	0.96	0.96
Loey [45] Loey, Manogaran & Khalifa, 2020.	0.88	0.78	0.85	0.83
He [46] (He, Yang et al. 2020)	–	–	–	0.86
Our method	**1.0000**	**0.98**	**1.0000**	**0.99**

Acknowledgement

Xiang Yu holds a CSC scholarship with the University of Leicester. The paper was partially supported by Royal Society International Exchanges Cost Share Award, UK (RP202G0230); Hope Foundation for Cancer Research, UK (RM60G0680); Medical Research Council Confidence in Concept Award, UK (MC_PC_17171); British Heart Foundation Accelerator Award, UK; Fundamental Research Funds for the Central Universities (CDLS-2020-03); Key Laboratory of Child Development and Learning Science (Southeast University), Ministry of Education; Guangxi Key Laboratory of Trusted Software (kx201901).

References

Abbas, A., Abdelsamea, M.M., .& Gaber, M.M. (.2020)"Classification of COVID-19 in chest X-ray images using DeTraC deep convolutional neural network," arXiv preprint arXiv:2003.13815.

Adhikari, N. C. D. (2020). Infection severity detection of CoVID19 from X-Rays and CT scans using artificial intelligence. *International Journal of Computer (IJC), 38*, 73–92.

Apostolopoulos, I. D., & Mpesiana, T. A. (2020). Covid-19: Automatic detection from x-ray images utilizing transfer learning with convolutional neural networks. *Physical and Engineering Sciences in Medicine, **43**,*, 635-640.

Behzadi, P., Ranjbar, R., & Alavian, S. M. (2014). Nucleic acid-based approaches for detection of viral hepatitis. *Jundishapur Journal of Microbiology, 8*, e17449. e17449.

Bukhari, S.U.K., Bukhari, S.S.K., Syed, A., & SHAH, S.S.H. (2020)"The diagnostic evaluation of convolutional neural network (CNN) for the assessment of chest X-ray of patients infected with COVID-19," medRxiv: 2020.2003.2026.20044610.

Chen, X., Chen, Y., Liu, H., Goldmacher, G., Roberts, C., Maria, D., et al. (2019). PIN92 Pediatric bacterial pneumonia classification through chest X-rays using transfer learning. *Value in Health, 22*, S209–S210.

(2020,. 2020). Chest X-Ray Images (Pneumonia). Available: https://www.kaggle.com/paultimothymooney/chest-xray-pneumonia.

Chollet, F. (2017). Xception: Deep learning with depthwise separable convolutions. In *Proceedings of the IEEE conference on computer vision and pattern recognition* (pp. 1251–1258).

Chowdhury, M.E., .Rahman, T., Khandakar, A., Mazhar, R., Kadir, M.A., .& Mahbub, Z.B. e.t al.,(2020) "Can AI help in screening viral and COVID-19 pneumonia?," arXiv preprint arXiv:2003.13145.

Chung, H., Park, J. G., & Jung, H. Y. (2019). Rank-weighted reconstruction feature for a robust deep neural network-based acoustic model. *ETRI Journal, 41*, 235–241.

Deng, J., Dong, W., Socher, R., Li, L.-. J., Li, K., & Fei-Fei, L. (2009). Imagenet: A large-scale hierarchical image database. In *IEEE conference on computer vision and pattern recognition, 2009* (pp. 248–255).

Fang, Y., Zhang, H., Xie, J., Lin, M., Ying, L., Pang, P., et al. (2020). Sensitivity of chest CT for COVID-19: Comparison to RT-PCR. *Radiology*, Article 200432.

He Kaiming, Z. X., Shaoqing, Ren, & Jian, S. (2016). Deep residual learning for image recognition. In *Proceedings of the IEEE conference on computer vision and pattern recognition* (pp. 770–778).

He, K., Zhang, X., Ren, S., & Sun, J. (2015). Delving deep into rectifiers: Surpassing human-level performance on imagenet classification. In *Proceedings of the IEEE international conference on computer vision* (pp. 1026–1034, Las Vegas Nevada).

He, K., Zhang, X., Ren, S., & Sun, J. (2016). Deep residual learning for image recognition. In *Proceedings of the IEEE conference on computer vision and pattern recognition* (pp. 770–778).

He, X., Yang, X., Zhang, S., Zhao, J., Zhang, Y., & Xing, E. et al.,(2020) "Sample-efficient deep learning for COVID-19 diagnosis based on CT scans," medRxiv,.doi: 10.1101/2020.04.13.20063941.

Huang, G., Liu, Z., Van Der Maaten, L., & Weinberger, K. Q. (2017). Densely connected convolutional networks. In *Proceedings of the IEEE conference on computer vision and pattern recognition (CVPR)* (pp. 4700–4708, Honolulu Hawaii, USA).

Iandola, F.N., .Han, S., Moskewicz, M.W., .Ashraf, K., Dally, W.J., .& a. p. a. Keutzer, K.J. (.2016)."SqueezeNet: AlexNet-level accuracy with 50x fewer parameters and< 0.5MB model size,"ArXiv **abs/1602.07360**.

Islam, K.T., .Wijewickrema, S., Collins, A., & O'Leary, S. (2020)."A deep transfer learning framework for pneumonia detection from chest X-ray images.", pp. 286-293. 10.5220/0008927002860293.

Jaiswal, A., Gianchandani, N., Singh, D., Kumar, V., & Kaur, M. (2020). Classification of the COVID-19 infected patients using DenseNet201 based deep transfer learning. *Journal of Biomolecular Structure and Dynamics*, 1–8.

Jia, Y., Shelhamer, E., Donahue, J., Karayev, S., Long, J., & Girshick, R. (2014). Caffe: Convolutional architecture for fast feature embedding. Proceedings of the 22nd ACM international conference on multimedia. *et al*, 675–678, doi: 10.1145/2647868.2654889.

Joaquin, A. (2020)."Using deep learning to detect pneumonia caused by NCOV-19 from X-ray images," ed, available at: https://towardsdatascience.com/using-deep-learning-to-detect-ncov-19-from-x-ray-images-1a89701d1acd.

Kermany, D. S., Goldbaum, M., Cai, W., Valentim, C. C., Liang, H., & Baxter, S. L. (2018). Identifying medical diagnoses and treatable diseases by image-based deep learning. *Cell, 172*, 1122–1131. e9.

Koo, H. J., Lim, S., Choe, J., Choi, S.-. H., Sung, H., & Do, K.-. H. (2018). Radiographic and CT features of viral pneumonia. *Radiographics : A Review Publication of the Radiological Society of North America, Inc, 38*, 719–739, 05/01, 2018.

Krizhevsky Alex, S. I., & H.G. E. (2012). Imagenet classification with deep convolutional neural networks. In *Advances in neural information processing systems* (pp. 1097–1105).

Li, K., Wu, J., Wu, F., Guo, D., Chen, L., Fang, Z., et al. (2020). The clinical and chest CT features associated with severe and critical COVID-19 pneumonia. *Investigative Radiology, 55*. https://doi.org/10.1097/RLI.0000000000000672.

Li, Z., Zhang, Z., Qin, J., Zhang, Z., & Shao, L. (2019). Discriminative fisher embedding dictionary learning algorithm for object recognition. *IEEE Transactions on Neural Networks and Learning Systems*. https://doi.org/10.1109/TNNLS.2019.2910146.

Liang, G., & Zheng, L. (2019). A transfer learning method with deep residual network for pediatric pneumonia diagnosis. *Computer Methods and Programs in Biomedicine*, Article 104964.

Liang, P., & Bose, N. (1996). *Neural network fundamentals with graphs, algorithms, and applications*. Mac Graw-Hill.

Loey, M., Manogaran, G., & Khalifa, N.E.M. (2020)."A deep transfer learning model with classical data augmentation and cgan to detect covid-19 from chest ct radiography digital images,", Preprints 2020040252.

Malagón-Borja, L., & Fuentes, O. (2009). Object detection using image reconstruction with PCA. *Image and Vision Computing, 27*, 2–9.

Rajpurkar, P., Irvin, J., Zhu, K., Yang, B., Mehta, H., & Duan, T. et al.,(2017) "Chexnet: Radiologist-level pneumonia detection on chest x-rays with deep learning," arXiv preprint arXiv:1711.05225.

Ronneberger, O., Fischer, P., & Brox, T. (2015). U-net: Convolutional networks for biomedical image segmentation. In *International conference on medical image computing and computer-assisted intervention* (pp. 234–241).

Shen, H. T., Zhu, X., Zhang, Z., Wang, S.-. H., Chen, Y., Xu, X., et al. (2021). Heterogeneous data fusion for predicting mild cognitive impairment conversion. *Information Fusion, 66*, 54–63, 2021/02/01/.

Simonyan Karen, Z.A. (.2014)"Very deep convolutional networks for large-scale image recognition," arXiv*preprint arXiv:1409.1556*.

Szegedy Christian, L. W., Jia, Yangqing, Sermanet, Pierre, Reed, Scott, Anguelov, Dragomir, & Erhan, Dumitru (2015). Going deeper with convolutions. In *Proceedings of the IEEE conference on computer vision and pattern recognition* (pp. 1–9).

Szegedy, C., Vanhoucke, V., Ioffe, S., Shlens, J., & Wojna, Z. (2016). Rethinking the inception architecture for computer vision. In *Proceedings of the IEEE conference on computer vision and pattern recognition* (pp. 2818–2826, Las Vegas Nevada, USA).

Wang, H., & Xia, Y. (2018)"Chestnet: A deep neural network for classification of thoracic diseases on chest radiography," arXiv preprint arXiv:1807.03058.

Wang, S., Kang, B., Ma, J., Zeng, X., Xiao, M., & Guo, J. et al.,(2020) "A deep learning algorithm using CT images to screen for corona virus disease (COVID-19)," MedRxiv,, doi: 10.1101/2020.02.14.20023028.

Wen, J., Zhang, Z., Zhang, Z., Fei, L., & Wang, M. (2020). Generalized incomplete multiview clustering with flexible locality structure diffusion. *IEEE Transactions on Cybernetics*. https://doi.org/10.1109/TCYB.2020.2987164.

Wu, Y.-.H., Gao, S.-.H., Mei, J., Xu, J., Fan, D.-.P., & Zhao, C.-.W. et al.,(2020) "JCS: An explainable COVID-19 diagnosis system by joint classification and segmentation," arXiv preprint arXiv:2004.07054.

Zhang, Z., Lai, Z., Huang, Z., Wong, W. K., Xie, G.-. S., Liu, L., et al. (2019). Scalable supervised asymmetric hashing with semantic and latent factor embedding. *IEEE Transactions on Image Processing, 28*, 4803–4818.

Zhang, Z., Liu, L., Luo, Y., Huang, Z., Shen, F., & Shen, H. T. (2020). Inductive structure consistent hashing via flexible semantic calibration. *IEEE Transactions on Neural Networks and Learning Systems*. https://doi.org/10.1109/TNNLS.2020.3018790.

Zhang, Z., Liu, L., Shen, F., Shen, H. T., & Shao, L. (2018). Binary multi-view clustering. *IEEE Transactions on Pattern Analysis and Machine Intelligence, 41*, 1774–1782.

Zhao, J., Zhang, Y., He, X., & Xie, P. (2020)"COVID-CT-Dataset: A CT scan dataset about COVID-19," arXiv preprint arXiv:2003.13865.

Zhao, Z.-. Q., Zheng, P., Xu, S.-t., & Wu, X. (2019). Object detection with deep learning: A review. *IEEE Transactions on Neural Networks and Learning Systems*. https://doi.org/10.1109/TNNLS.2018.2876865.